

Contents lists available at ScienceDirect

Deep-Sea Research Part I

journal homepage: www.elsevier.com/locate/dsri





Physical drivers of sediment-water interaction on the Beaufort Sea shelf

Jessica S. Dabrowski ^a, Robert S. Pickart ^a, Dean A. Stockwell ^b, Peigen Lin ^a, Matthew A. Charette ^{a,*}

- ^a Woods Hole Oceanographic Institution, Woods Hole, MA, USA
- ^b University of Alaska Fairbanks, Fairbanks, AK, USA

ARTICLE INFO

Keywords:
Arctic ocean
Radium isotopes
Nutrients
Polynya
Sediment-water exchange
Winter water

ABSTRACT

Climate change is causing sea ice loss on Arctic continental shelves, resulting in increases of shelf-derived materials to the Arctic Ocean. Sediment-water interaction can chemically transform water as it moves across the shelf, enriching shelf waters in nutrients and carbon, which can impact primary productivity and greenhouse gas cycling. However, the drivers of sediment-water interaction in the Arctic Ocean are poorly understood. In this study, we use radium isotope measurements and physical data from a cruise to the Beaufort shelf in late-October-November 2018 to investigate the impact of storm events and winter water formation on sediment-water interaction. In response to winter water formation, radium-228 and ²²⁸Ra/²²⁶Ra increased in shelf bottom waters, with both indicative of enhanced sediment-water exchange. Ammonium, an important nutrient for phytoplankton growth with a known sediment source, also increased during this time period. Our results suggest that processes related to ice formation, together with wind effects, have the ability to drive dissolved constituents from sediment porewaters into the water column. The spatial variability in chemical constituents and water mass ages based on short-lived Ra isotopes suggest that these sediment-water interaction events are episodic in nature, and that storm-driven mesoscale water column features can drive local exchange with the benthos.

1. Introduction

The Arctic Ocean is strongly influenced by continental shelves, which make up 50% of its area (Jakobsson, 2002). Climate warming is causing sea ice loss over shelves, allowing for increased vertical mixing and shelf-basin exchange (Carmack and Chapman, 2003; Rainville et al., 2011; Williams and Carmack, 2015). In the past two decades, increases in shelf-derived materials have been observed in the central Arctic (Kipp et al., 2018; Rutgers van der Loeff et al., 2018). These material inputs are in part due to sediment-water interactions (SWIs), which chemically transform water as it moves across the shelf, transferring nutrients, carbon, and trace metals from sediments into the water column (Codispoti et al., 2005, 2009; Brown et al., 2015; Shen et al., 2016; Vieira et al., 2019). Because these inputs can influence biological productivity and greenhouse gas cycling, it is important to understand the drivers of SWI on Arctic continental shelves.

During late autumn through early spring, shelf water is transformed physically and chemically via ice formation that rejects brine and causes vertical convection, creating an Arctic water mass known as Newly Ventilated Winter Water (WW, e.g. Pacini et al., 2019). This cold water,

near the freezing point, is rich in nutrients and trace metals due to interaction with the sediments (Granger et al., 2018; Jones and Anderson, 1986; Vieira et al., 2019). Winter water is known to form within large, semi-permanent polynyas (Itoh et al., 2012; Pickart et al., 2016; Weingartner et al., 1998) and in small leads and polynyas throughout the Chukchi Sea (Pacini et al., 2019), which ultimately exits the shelf and ventilates the upper halocline of the Arctic Ocean (Aagaard et al., 1981). However, little is known about WW formation in late autumn and its effect on SWI, in part due to the lack of shipboard measurements that time of year.

The nutrients released from bottom sediments, such as dissolved inorganic nitrogen and trace metals, are involved in numerous biogeochemical cycling processes (Bruland and Lohan, 2003; Cid et al., 2012; Cota et al., 1996; Lee et al., 2010; Tremblay et al., 2006), making it difficult to use them as tracers of SWI processes. In the case of ammonium (NH₄⁺), its water column residence time once released from shelf sediments is controlled by a host of factors, including salinity, light and pH (Heiss and Fulweiler, 2016). However, naturally occurring radium isotopes (223 Ra, $^{1/2}$ = 11.4 d; 224 Ra, $^{1/2}$ = 3.66 d; 226 Ra, $^{1/2}$ = 1600 y; 228 Ra, $^{1/2}$ = 5.75 y), are similarly sourced and behave conservatively on

E-mail address: mcharette@whoi.edu (M.A. Charette).

^{*} Corresponding author.

the time scales of shelf circulation. They are produced through the decay of sediment-bound thorium isotopes, and because of their higher solubility, dissolve into bottom sediment porewaters, which can then be released through diffusive processes (Charette et al., 2008; Webster et al., 1995) or bioirrigation, bioturbation, and physical transport of sediment (Santos et al., 2012; Burt et al., 2014; Rodellas et al., 2015). Radium isotopes can also enter the coastal ocean through river runoff or submarine groundwater discharge (Moore, 2010; Mulligan and Charette, 2006; Rutgers van der Loeff et al., 2003). Radium then is lost to decay based on its half-life and dilution through mixing with open-ocean waters (Charette et al., 2008). ²²⁸Ra has been well utilized as a tracer of shelf waters influenced by sediments in the Arctic (Charette et al., 2020; Kipp et al., 2020; Rutgers van der Loeff et al., 1995, 2012, 2018), but

comparatively less shelf-based work has employed the use of the short-lived radium isotopes to observe SWI on shorter timescales of days to weeks (Cai et al., 2014, 2015; Shi et al., 2019).

Here, we combine physical and chemical observations from an autumn field program in late-October to mid-November 2018 to elucidate the influence of wind-driven and ice-formation-driven vertical convection and SWI on the Beaufort shelf. We first describe the atmospheric and sea ice conditions during the cruise, followed by an analysis of the hydrographic data as they relate to the water column response to storms and ice formation. We then present water column measurements of radium isotopes and ammonium, a common form of inorganic nitrogen in marine sediments, along with sedimentary measurements of radium isotopes to inform the water column observations. Finally, we

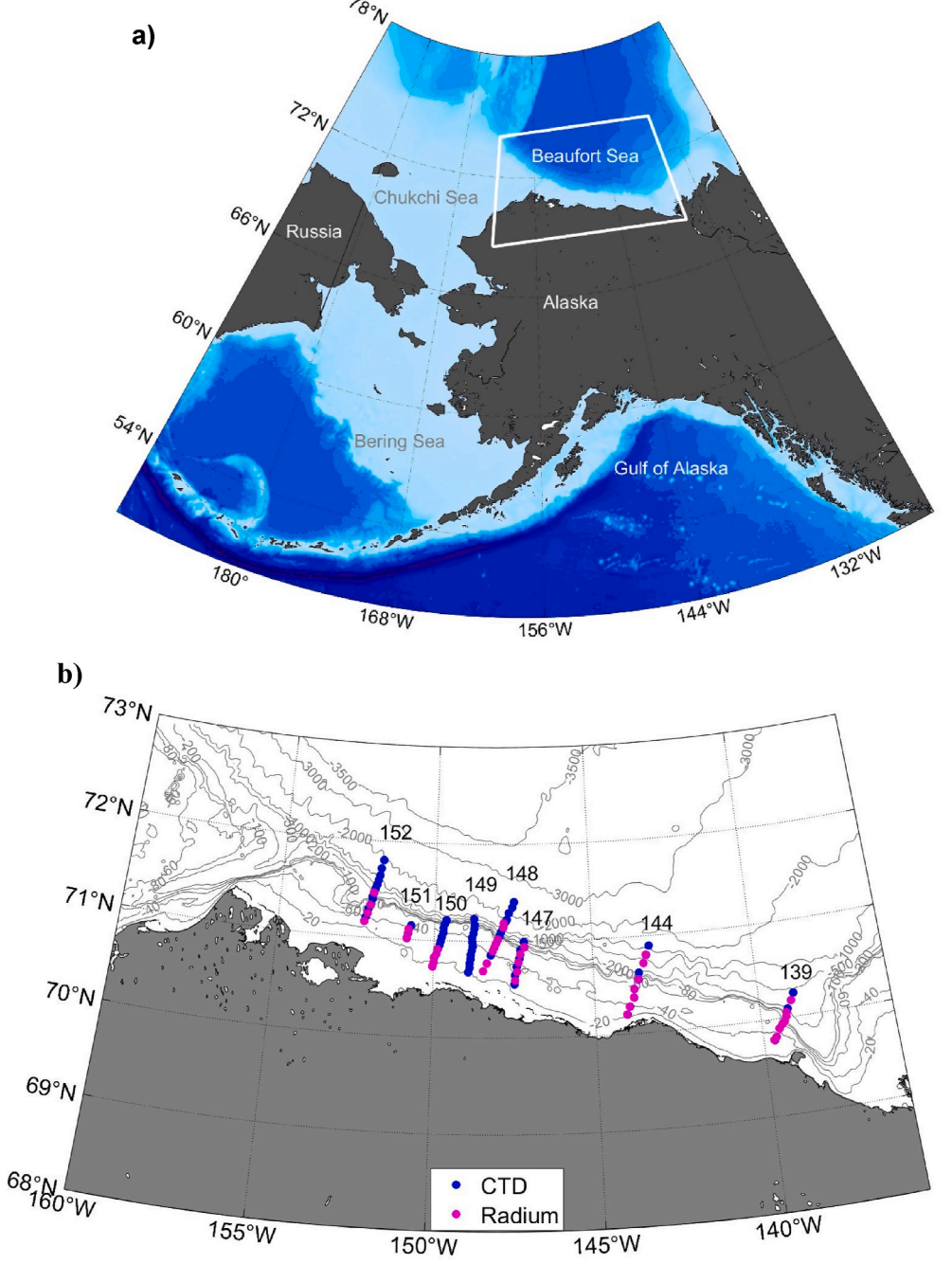


Fig. 1. (a) Map of the study area and schematic circulation of the Chukchi and western Beaufort seas, with place names (after Corlett and Pickart, 2017). The sampling area is highlighted by the white box. (b) Locations of sampling stations during HLY 1803, Oct–Nov 2018. Conductivity-temperature-depth (CTD) stations are shown in blue. CTD/Radium stations are shown in magenta. The sections are labeled by their approximate longitude.

discuss a timeseries of storm events and WW formation during three periods in early November across the Beaufort shelf, and use chemical evidence to investigate the extent of SWI as WW forms and spreads.

2. Study area

The Chukchi and Beaufort continental shelves of the Arctic are characterized as inflow shelves due to inflow of Pacific Water through Bering Strait (Williams and Carmack, 2015). This water is transported across the Chukchi shelf, and some of it turns to the east after exiting Barrow canyon to form the Beaufort Shelfbreak Jet (Fig. 1a, Nikolopoulos et al., 2009; Pickart, 2004). This eastward flow can be temporarily reversed during wind-driven upwelling events (Pickart et al., 2009, 2011, 2013a), or be strengthened during wind-driven downwelling (Foukal et al., 2019). The upwelling is often associated with low pressure systems passing over the Aleutian Islands, which, in combination with the Beaufort High, a quasi-stationary high-pressure system over the Beaufort Sea (Walsh, 1978), cause strong easterly winds in the Beaufort Sea (e.g. Pickart et al., 2009; Lin et al., 2019).

The upwelling at the shelfbreak is most common in autumn (Lin et al., 2019), with an increase in frequency in recent years (Pickart et al., 2013b). When winds exceed 4–5 m s⁻¹ for at least 6–18 h, the along-shelf flow reverses to the west, followed roughly 10 h later by upwelling of water from the halocline. Outside of the summer months, the majority of the events bring warm, salty, nutrient-rich Atlantic Water onto the shelf (Lin et al., 2019). Downwelling occurs when cyclonic low-pressure systems transit through the Canada Basin, leading to strong westerly winds over the region. This occurs most commonly in July and August (Foukal et al., 2019). It leads to an acceleration of the shelfbreak jet, followed roughly 10 h later by downwelling of near-bottom water off the Beaufort shelf that ventilates the upper halocline of the Canada Basin.

In this study, we collected samples during the autumn freeze-up in 2018 across much of the Alaskan Beaufort shelf between the eastern Chukchi Sea and Mackenzie Canyon. The focus of the paper is on the set of samples from the central Beaufort shelf (145-150°W; Fig. 1b). The two transects to the west were excluded because one of them was taken early in the cruise before WW was being formed (section 152, Fig. 1b), while the other section was halted after only four stations (section 151). We also excluded the transect farthest to the east near Mackenzie Canyon (section 139) since local canyon dynamics were likely influencing that section. We occupied multiple hydrographic sections between 145 and 150°W over two weeks in early November. In terms of SWI, the mineral and organic carbon content of the sediments is relatively consistent from east to west in this portion of the Alaskan Beaufort Sea, with some inner to outer shelf gradients in terrestrial organic matter sources (Goñi et al., 2013; Naidu et al., 2000; Naidu and Mowatt, 1983), so we assume that benthic sources of radium isotopes and nutrients do not vary strongly between transects. The paper is further divided into three sampling periods based on easterly wind events and progressive cooling of the water column with time due to sea ice and WW formation. Period 1 (Oct 30-Nov 1) is characterized by a short, easterly wind event at the early stages of WW formation on the inner shelf. In period 2 (Nov 3-7), a strong, easterly wind event extends over several days associated with further ice formation. During period 3 (Nov 10-14), a weaker easterly wind event occurs as average sea ice concentrations increase to nearly 100% on the shelf, while the presence of WW continues to increase.

3. Methods

3.1. Sample collection and analysis

Samples were collected from October 25 – November 19, 2018 aboard USCGC *Healy* cruise HLY 1803. A total of 196 stations were occupied along 19 transects, a subset of which we present in Fig. 1b. At

all stations, hydrographic data were collected using a Sea-Bird 911+ conductivity-temperature-depth (CTD) system, configured to measure pressure, temperature, conductivity and beam transmission on a 24-position rosette with 12-L bottles. A laboratory calibration of the temperature, conductivity, and beam transmission sensors was done before and after the cruise, and an in-situ calibration of the conductivity sensors was carried out during the cruise via bottle salinity measurements. Accuracies were determined to be 0.001 °C for temperature and 0.002 for salinity (practical salinity). Vertical sections were constructed using a Laplacian-spline interpolation scheme with a typical grid spacing of 5 km and 2 m, in the horizontal and vertical, respectively. The variables considered are potential temperature referenced to the sea surface (hereafter referred to simply as temperature), salinity, and potential density referenced to the sea surface (hereafter referred to as density).

Velocity of the water column was measured using *Healy's* hull-mounted RDI Ocean Surveyor 150 kHz acoustic Doppler current profiler (ADCP). Data coverage was typically from 18 m depth to approximately 10 m above the seafloor on the shelf. Because of the presence of sea ice, most ADCP profiles were collected while on station. The data were processed following the procedure described in Pickart et al. (2016). Barotropic tidal signals were removed using the Oregon State University model (Padman and Erofeeva, 2004). We note that the tidal signals on the Beaufort shelf/slope are very small. Based on a mooring array deployed in the study region, the amplitude of the four primary tidal constituents is less than 0.015 m s⁻¹, an order of magnitude smaller than the wind and buoyancy-driven horizontal flows. Absolute geostrophic velocity sections were made by referencing the thermal wind shear to the direct ADCP measurements following Pickart et al. (2016).

Samples (~250 L) for radium isotopes were collected at 72 stations using Niskin bottles on the CTD rosette. At shelf stations, samples were collected 4-7 m above the seafloor in order to focus on the influence of SWI. On the slope, samples were collected in the same potential density range as the bottom water on the shelf to maximize the chance of sampling the same water masses on and off the shelf. Surface water samples were collected for comparison with bottom water samples. Samples were pre-filtered through 10 µm and 1 µm Hytrex cartridges and transferred to plastic barrels. The samples were then filtered at \sim 1 L min⁻¹ through MnO₂-coated acrylic fibers to quantitatively capture radium (Moore and Reid, 1973). Fibers were rinsed with radium-free deionized water and dried partially with filtered air prior to analysis for short-lived isotopes (223Ra, 224Ra) on the Radium Delayed Coincidence Counter (RaDeCC) system (Moore and Arnold, 1996). Initial analyses were performed on the ship within 3 days of collection; samples were further analyzed in the lab after 1 and 2 months to determine the ²²⁴Ra and ²²³Ra activities supported by ²²⁸Th and ²²⁷Ac, respectively; therefore, all reported values of ²²⁴Ra and ²²³Ra are excess (²²⁴Ra_{ex} and ²²³Ra are excess) ²²³Ra_{ex}) activities in the water column not supported by their parents.

For analysis of long-lived radium isotopes, fibers were ashed in a muffle furnace at 820 $^{\circ}\text{C}$ for 24 h. The ash was sealed in polystyrene vials with epoxy (to prevent ^{222}Rn loss), stored for at least 1 month to allow for daughter-product ingrowth, and counted on a high-purity, well-type germanium gamma detector to measure ^{228}Ra and ^{226}Ra using the spectral lines for ^{228}Ac (338 and 911 keV) and ^{214}Pb (352 keV), respectively. Detector efficiencies were determined using standards prepared in the same geometry as the samples. Analytical uncertainties for all radium isotopes are reported as 1σ .

At most of the hydrographic stations, nutrient samples were collected from Niskin bottles at $\sim\!10$ m intervals. These samples were not filtered due to relatively low particulate load during the cruise. Samples were frozen until analysis at the University of Alaska using a Seal Analytical continuous-flow QuAAtro39 AutoAnalyzer. Following each run, the data were manually inspected, any blank was subtracted, and final concentrations were calculated based on a linear curve fit using Seal Analytical AACE 7.07 software. Reagent solutions and primary and secondary standards were prepared with fresh Milli-Q water and

working standards were prepared daily with low nutrient artificial seawater and primary standards with >99% purity from Fisher Scientific and/or VWR. A second set of nutrient samples was collected coincident with radium samples, after pre-filtering but prior to plastic barrel storage. These samples were similarly analyzed at the Woods Hole Oceanographic Institution Nutrient Analytical Facility using a four-channel segmented flow Seal AA3 HR Autoanalyzer. The detection limits for $\mathrm{NH_4}^+$ was ${\sim}0.015~\mu\mathrm{M}$ for both sets of nutrient analyses.

Bulk surface sediments (upper 5-10 cm) were collected at 28 of the hydrographic stations using a van Veen Grab. Sediments were stored in clean plastic bags and kept frozen until analysis. Sediments were weighed, dried, then re-weighed to determine water content and porosity assuming a mineral grain density of 2.65 g \mbox{cm}^{-3} and corrected for sea salt. Aliquots of these sediment samples were analyzed for radium isotopes. Surface available ²²³Ra and ²²⁴Ra were measured using a modified procedure described by Cai et al. (2012). MilliQ water was added to dried, weighed sediments to form a slurry, followed by co-precipitation of any desorbed radium, thorium or actinium by MnO₂ suspension. The precipitate and sediments were filtered onto a 142 mm 0.7 µm GFF filter, and analyzed in a sample chamber in the same geometry as the standards. In addition to creating a²²⁸Th set of standards for ²²⁴Ra, a set of standards was also made for ²²³Ra by spiking sediments with a²²⁷Ac solution. A set of filter standards and sediment standards were made for each transect to determine efficiencies based on sediment type. We ensured that moisture content and radioisotope counts were stable during the measurement. Values are reported as averages and standard deviations of at least 3 measurements. Bulk Ra isotopes were measured via gamma spectrometry as described above using 4-5 g of dried sediment packed into polystyrene vials. ²²⁸Ra and ²²⁶Ra were measured relative to a sediment standard (Certified Reference Material: IAEA-385). Analytical uncertainties are reported as 1σ .

3.2. Meteorological and sea ice data

To investigate the impacts of storm events during the cruise, we use sea level pressure (SLP) and 10-m wind speed data from the ECMWF Integrated Forecast System (IFS) ERA5 reanalysis product (Hersbach and Dee, 2016). The spatial and temporal resolution are 0.25° and 1 h, respectively. As a check on the accuracy of the ERA5 wind data, we extracted the timeseries at the grid point closest to the Barrow Atmospheric Baseline Observatory (BABO; https://www.esrl.noaa.gov/gmd/obop/brw/) near Utqiagvik (formerly known as Barrow). The agreement between the two independent datasets was excellent. Fig. 2a shows the alongcoast windspeed from BABO, where the positive alongcoast direction is 105° true. As shown by Nikolopoulos et al. (2009), the alongcoast winds are most highly correlated with the currents on the Beaufort shelf and slope. The 2-m air temperature measured at BABO indicates that temperatures were less than 0 °C throughout the study period (Fig. 2b).

We use the Advanced Microwave Scanning Radiometer 2 (AMSR-2) data to characterize sea ice concentration over the shelf in autumn of 2018. AMSR-2 has a 3.125 km spatial resolution in our study region and daily temporal resolution. The data originate from the Global Change Observation Mission 1st-Water satellite, which measures seven frequency bands from 6.925 to 89.0 GHz (Beitsch et al., 2014). The data were downloaded from the University of Bremen (http://www.iup.uni-bremen.de:8084/amsr2data/asi_daygrid_swath/n6250/2014/).

4. Results

This study centers around three storm events in November 2018. As noted in the introduction, upwelling events in the Beaufort Sea are most common in Oct–Nov (Lin et al., 2019; Pickart et al., 2013b), and this year was no exception. The three events were defined using the along-coast wind record, which were used to organize the hydrographic data into three periods (Fig. 2a). Period 1 was from Oct 30-Nov 1, period 2 from Nov 3–7, and period 3 from Nov 10–14. We first examine the atmospheric conditions during the events followed by characterization of the sea ice concentration and the occurrence of polynyas on the shelf. We then contrast the hydrographic conditions associated with these periods on the central Beaufort shelf, followed by radium isotopes and nutrients in the water column (Table 1). Finally, radium isotopes in the

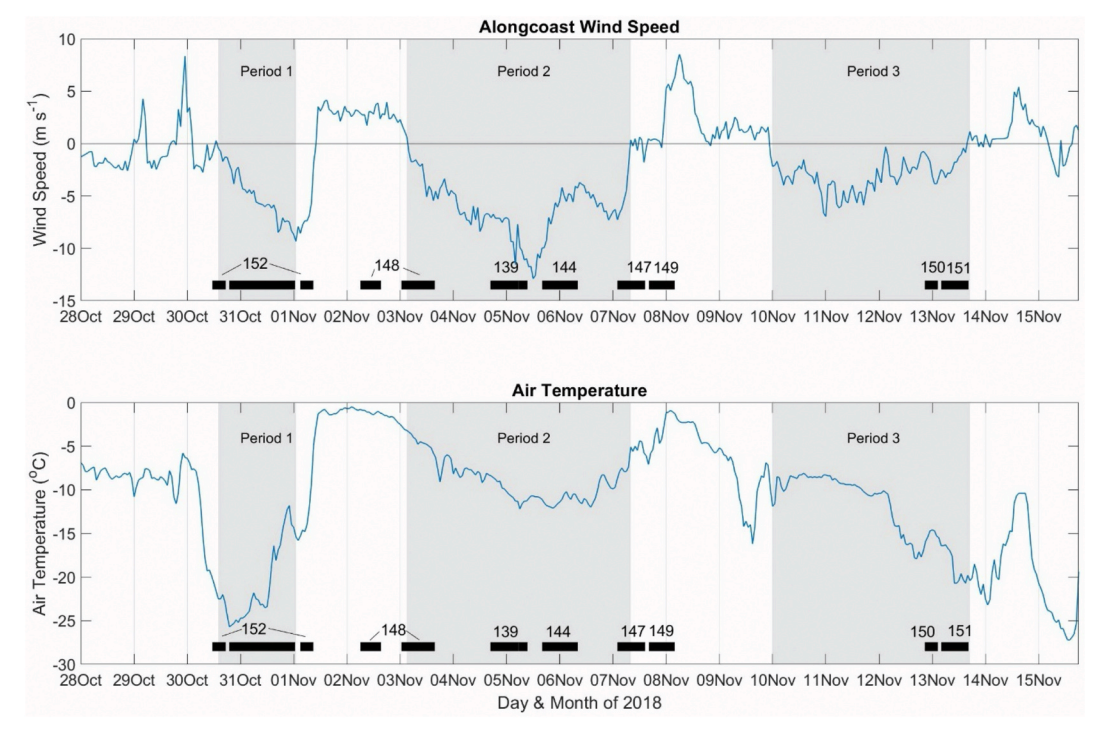


Fig. 2. (a) Alongcoast wind speed from the Barrow Atmospheric Baseline Observatory. The grey shading indicates the three upwelling events. The black bars at the bottom mark the time of occupation of the hydrographic sections (labeled by longitude). The reason for the breaks in sections 152 and 148 is that mooring work interrupted the occupation of these two sections. (b) Air-temperature at 2 m above sea level measured at the Barrow Atmospheric Baseline Observatory.

Table 1
Radium isotope and ammonium data from cruise HLY 1803, Oct–Nov 2018. Period 1 stations were those collected on Nov. 2–3, while Period 2 and Period 3 correspond to Nov. 7 and Nov. 12–13 stations, respectively.

Transect-station name	Sample Collection Date	Latitude (°N)	Longitude (°W)	Depth	Salinity	²²⁴ Ra _{xs}	+/-	$^{223}\mathrm{Ra}_{\mathrm{xs}}$	+/-	²²⁶ Ra	+/-	²²⁸ Ra	+/-	MH4 ⁺ μmol L ⁻¹
				(m)					dpm 10	$0 \; \mathrm{L}^{-1}$				
DBO6-1	10/30/18	71.1644	152.2523	24.4	31.8990	5.64	0.28	0.28	0.03	11.91	0.12	12.06	0.46	1.45
DBO6-3	10/30/18	71.2483	152.1632	1	31.1028	2.85	0.25	0.15	0.03	11.18	0.28	9.40	0.52	0.97
DBO6-3	10/30/18	71.2483	152.1632	41.2	32.2296	6.16	0.33	0.12	0.03	12.25	0.26	10.75	0.49	1.84
DBO6-5	10/31/18	71.3357	152.0953	1	29.4519	1.50	0.20	0.03	0.02	10.74	0.12	7.32	0.41	1.69
DBO6-7	10/31/18	71.4203	152.0388	63.1	32.3553	6.67	0.26	0.06	0.02	12.00	0.21	9.95	0.37	1.10
DBO6-8	10/31/18	71.4625	152.0020	120.2	32.7090	1.51	0.22	0.02	0.01	13.83	0.12	9.50	0.39	ND
DBO6-8	10/31/18	71.4613	151.9938	45.6	31.4556	0.86	0.31	ND	ND	11.73	0.22	9.58	0.37	0.29
DBO6-19	11/1/18	72.6627	150.8792	55.2	29.7900	2.82	0.19	0.03	0.02	10.54	0.11	5.78	0.35	0.57
PRB-1	11/2/18	70.6915	148.4433	20.5	31.6520	4.31	0.27	0.22	0.03	12.38	0.12	9.92	0.41	0.07
PRB-2	11/2/18	70.7718	148.3257	2.5	31.4600	2.86	0.20	0.09	0.03	12.20	0.14	8.26	0.53	0.73
PRB-4	11/2/18	70.8975	148.1432	36.2	31.6828	5.66	0.23	0.23	0.03	12.12	0.25	9.49	0.43	0.53
PRB-5	11/2/18	70.9385	148.0883	2.5	31.1746	1.56	0.28	0.02	0.03	11.37	0.18	7.74	0.63	0.74
PRB-6	11/2/18	70.9778	148.0378	2.5	31.1555	0.99	0.28	0.08	0.03	11.60	0.29	8.24	0.48	0.61
PRB-7	11/2/18	71.0197	147.9743	51.6	32.0260	5.94	0.24	0.09	0.02	11.80	0.16	8.21	0.59	0.03
PRB-10	11/3/18	71.1465	147.8031	110.4	32.5856	2.98	0.23	ND	ND	11.67	0.13	ND	ND	ND
PRB-10	11/3/18	71.1427	147.8128	60.5	31.6602	1.05	0.21	0.01	0.01	11.69	0.14	7.74	0.42	0.48
PRB-11	11/3/18	71.1864	147.7932	3.2	26.3164	1.13	0.25	0.00	0.02	10.81	0.21	8.38	0.36	0.18
MCK-1	11/4/18	69.8165	139.6102	34.1	32.6493	10.62	0.33	0.20	0.04	12.77	0.13	7.62	0.43	0.16
MCK-2	11/4/18	69.8987	139.4943	37	32.5384	7.91	0.22	0.18	0.03	3.40	0.08	2.50	0.28	0.41
MCK-3	11/4/18	69.9398	139.3867	2.5	26.5525	0.77	0.27	0.11	0.03	22.90	0.17	12.91	0.52	0.66
MCK-4	11/4/18	69.9673	139.2998	52.1	32.2923	5.43	0.24	0.15	0.03	12.23	0.25	7.29	0.39	0.85
MCK-5	11/4/18	70.0122	139.2383	2.5	26.2651	0.95	0.28	ND	ND	9.52	0.18	6.45	0.66	0.37
KTO-1	11/5/18	70.2011	144.0332	20.3	32.3533	5.98	0.32	0.34	0.05	14.25	0.13	9.94	0.41	1.15
KTO-2	11/5/18	70.2824	143.9398	30.7	32.1526	4.05	0.25	0.15	0.03	11.84	0.09	7.90	0.34	1.47
KTO-3	11/5/18	70.3731	143.7918	2.5	31.4187	4.71	0.25	ND	ND	12.26	0.32	7.80	0.53	1.07
KTO-4	11/5/18	70.4596	143.7609	43.8	32.1259	4.78	0.26	0.09	0.03	12.00	0.12	7.46	0.40	1.04
CTO-5	11/5/18	70.5571	143.6240	2.5	27.3036	0.67	0.27	0.09	0.03	11.68	0.19	10.04	0.69	1.47
MCK-0	11/5/18	69.7877	139.6896	2.5	31.7549	2.48	0.25	0.07	0.03	12.78	0.14	7.26	0.51	1.46
MCK-6	11/5/18	70.0558	139.2133	50.3	31.4213	2.31	0.21	0.01	0.02	11.19	0.12	7.04	0.40	0.49
MCK-8	11/5/18	70.1713	139.0298	2.9	25.4135	1.22	0.21	0.00	0.01	10.44	0.13	7.86	0.43	1.71
KTO-7	11/6/18	70.7200 70.8058	143.4248	55.9	31.3673	2.25	0.32	0.09	0.02	10.78	0.08	6.66	0.28	0.29
KTO-8 PRE-10	11/6/18	70.8058	143.3360 147.4454	2.5 29.4	25.4777 31.7757	1.13 3.91	0.30 0.47	0.05 0.21	0.02 0.03	11.18 12.91	0.12 0.08	7.84 8.69	0.38 0.26	0.80
PRE-2	11/7/18 11/7/18	70.3942	147.1427	93	32.3632	6.41	0.47	0.21	0.03	13.12	0.08	9.13	0.20	1.15
PRE-4	11/7/18	70.9402	147.2734	44.5	31.9887	2.91	0.20	0.00	0.02	12.39	0.13	7.95	0.41	1.13
PRE-6	11/7/18	70.7814	147.3360	39.4	32.0610	8.83	0.50	0.03	0.02	12.39	0.12	8.47	0.30	1.87
PRE-8	11/7/18	70.7814	147.3807	35.1	31.8156	6.14	0.49	0.23	0.04	12.00	0.10	8.91	0.33	0.98
OS2-1	11/9/18	71.4965	154.4544	31.3	31.5242	5.41	0.49	0.15	0.03	13.38	0.09	14.83	0.52	0.00
OS2-10	11/9/18	72.0961	154.5922	70	31.7059	0.44	0.41	0.23	0.03	11.69	0.14	10.75	0.86	1.97
OS2-10	11/9/18	71.5594	154.4950	31.5	31.3285	4.00	0.15	0.04	0.02	12.74	0.21	14.46	0.38	1.84
OS2-3	11/9/18	71.6276	154.4993	3.2	31.1045	0.72	0.34	0.23	0.03	11.82	0.13	14.68	0.61	2.08
OS2-4	11/9/18	71.6938	154.5087	44.7	31.4011	3.02	0.34	0.23	0.03	13.02	0.15	15.90	0.49	2.04
OS2-6	11/9/18	71.8288	154.5264	2.6	30.9139	2.06	0.26	0.25	0.03	11.50	0.13	11.85	0.49	1.70
OS2-8	11/9/18	71.9612	154.5738	55	31.6877	1.30	0.23	0.03	0.02	12.64	0.13	14.03	0.75	2.27
OS2-9	11/9/18	72.0318	154.5990	3.3	29.3451	0.87	0.23	ND	ND	10.08	0.20	7.72	0.73	2.02
OS4-1	11/10/18	71.9512	156.5834	67.1	32.4212	3.93	0.17	0.16	0.04	15.06	0.23	15.78	0.46	2.63
OS4-1	11/10/18	72.0120	156.6026	2.8	30.3876	0.83	0.30	0.10	0.04	11.21	0.24	13.80	0.46	1.65
OS4-3	11/10/18	72.0781	156.6108	68.2	32.2796	1.08	0.30	0.05	0.03	14.64	0.09	15.10	0.34	2.43
OS4-4	11/10/18	72.1460	156.6091	85.5	32.3137	ND	ND	ND	ND	13.89	0.10	14.70	0.41	4.06
OS4-5	11/10/18	72.2093	156.6050	3.3	29.9083	1.17	0.22	0.02	0.02	10.41	0.26	9.00	0.45	1.84
OS4-6	11/10/18	72.2850	156.6292	85.5	32.2227	0.39	0.28	0.06	0.02	13.87	0.14	14.02	0.51	1.63
OS4-9	11/10/18	72.4879	156.6255	120.2	32.3808	1.09	0.27	0.13	0.02	14.12	0.24	13.77	0.43	2.50
BW1-1	11/12/18	71.0133	150.8731	17.2	31.6715	15.06	0.58	ND	ND	13.86	0.11	10.83	0.41	0.56
3W1-2	11/12/18	71.0649	150.8420	2.9	31.3618	7.73	0.52	0.34	0.04	13.13	0.13	10.77	0.45	1.23
BW0-1	11/13/18	70.7316	150.0305	14.1	30.2067	6.56	0.56	0.30	0.05	13.48	0.16	11.04	0.57	1.91
BW0-2	11/13/18	70.7762	149.9926	15.3	31.7541	3.52	0.51	0.24	0.04	12.64	0.14	11.56	0.63	2.04
sW0-3	11/13/18	70.8236	149.9918	17.7	31.7706	3.86	0.53	0.20	0.03	12.80	0.09	10.81	0.34	3.65
SW0-4	11/13/18	70.8642	149.9178	4.1	31.7388	3.28	0.46	0.08	0.02	12.44	0.08	9.69	0.28	0.94
W0-5	11/13/18	70.9104	149.8894	21	31.6098	3.66	0.46	0.28	0.04	12.70	0.08	9.01	0.30	0.94
W1-3	11/13/18	71.1093	150.8265	23.8	31.3365	4.22	0.50	0.13	0.04	12.39	0.29	10.75	0.55	1.31
DBO5-1	11/14/18	71.2534	157.1377	40.5	34.5344	8.01	0.21	0.01	0.01	9.42	0.07	2.73	0.20	1.15
DBO5-10	11/14/18	71.6220	157.9277	57.1	32.3472	5.66	0.29	0.30	0.04	12.04	0.24	13.05	0.45	3.77
DBO5-2	11/14/18	71.2835	157.2417	2.4	30.3828	2.78	0.27	0.19	0.03	11.77	0.15	11.41	0.60	2.14
DBO5-4	11/14/18	71.3688	157.3836	53.4	32.8138	2.13	0.24	0.32	0.04	13.68	0.10	12.30	0.17	2.44
DBO5-6	11/14/18	71.4599	157.5911	60	32.6896	2.96	0.25	0.06	0.02	13.43	0.05	9.68	0.17	2.37
DBO5-8	11/14/18	71.5373	157.7538	3.4	29.9642	0.31	0.31	0.08	0.02	11.03	0.04	12.90	0.17	2.70
DBO5-9	11/14/18	71.5798	157.8332	59.1	32.3040	3.47	0.58	0.20	0.04	15.35	0.21	17.11	0.82	4.06
DBO3-2	11/15/18	68.2467	167.1279	39	31.3052	8.83	0.34	0.33	0.04	15.97	0.15	18.42	0.56	3.48
DBO3-5	11/15/18	68.0127	167.8771	2.8	30.2920	2.07	0.30	0.23	0.04	12.53	0.13	14.11	0.47	4.32
DBO3-7	11/15/18	67.7832	168.5888	45.5	32.5298	6.52	0.38	0.64	0.06	14.91	0.13	13.91	0.50	4.82

shelf sediments are presented and compared to water column values to calculate time since SWI.

4.1. Wind events and sea ice concentration

To understand the atmospheric circulation during the three events, we constructed wind vector maps for each period. Fig. 3 shows a snapshot of the wind field for a given day in each of the three periods (which are representative of the entire period in question). Each event was associated with easterly winds, though the strongest easterlies were recorded during period 2 (Fig. 3b). The wind threshold for upwelling

(4–5 m s⁻¹; Pickart et al., 2009) was reached in each of the cases (Fig. 3). During period 2 it exceeded 10 m s⁻¹, which only occurs in about 25% of the storms in this region (Schulze and Pickart, 2012).

Throughout the cruise, sea ice covered much of the Beaufort Sea and shelf. As discussed above, WW formation occurs due to refreezing in polynyas and leads (e.g. Jackson et al., 2015; Pacini et al., 2019). While WW formation is not restricted to periods of upwelling, easterly winds on the Beaufort shelf/slope tend to open up leads and polynyas in the ice, which leads to more extensive WW formation. Here we define polynyas as areas where the ice concentration is <80%. Fig. 3 includes the polynya presence for the three cases. During period 1, polynyas existed

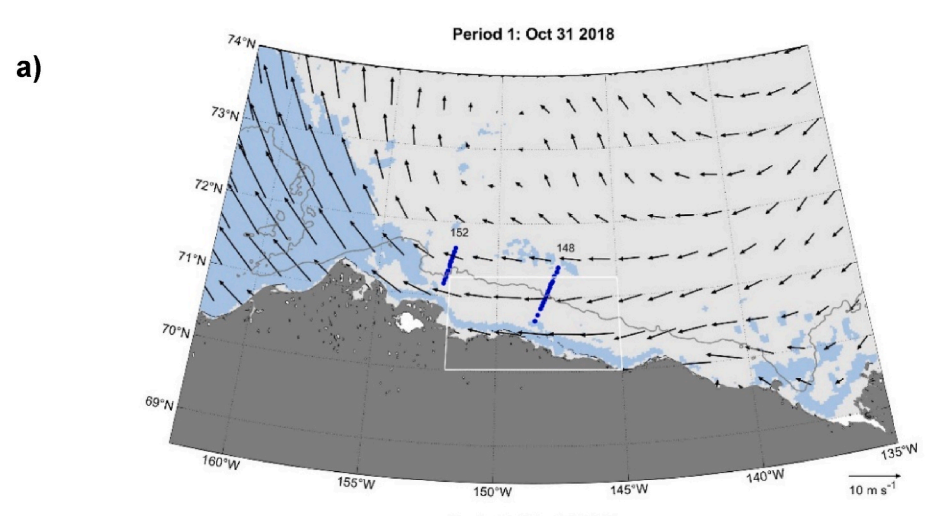
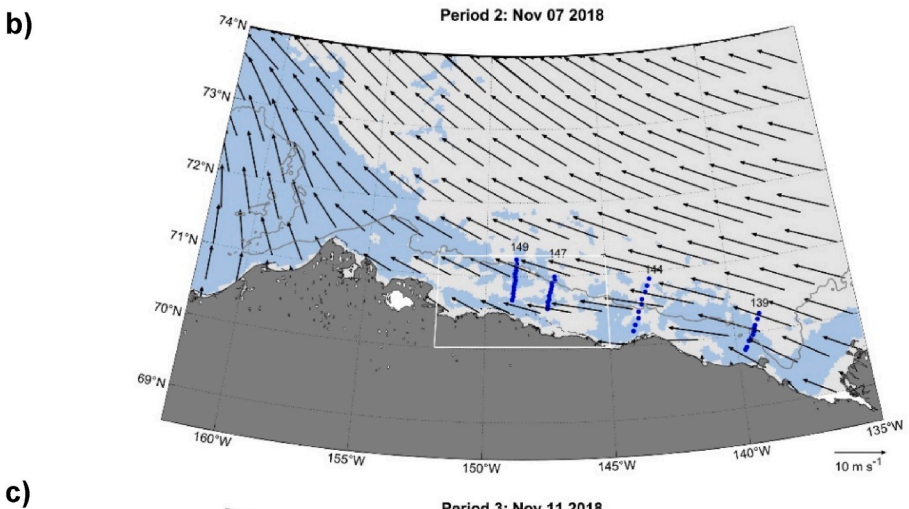
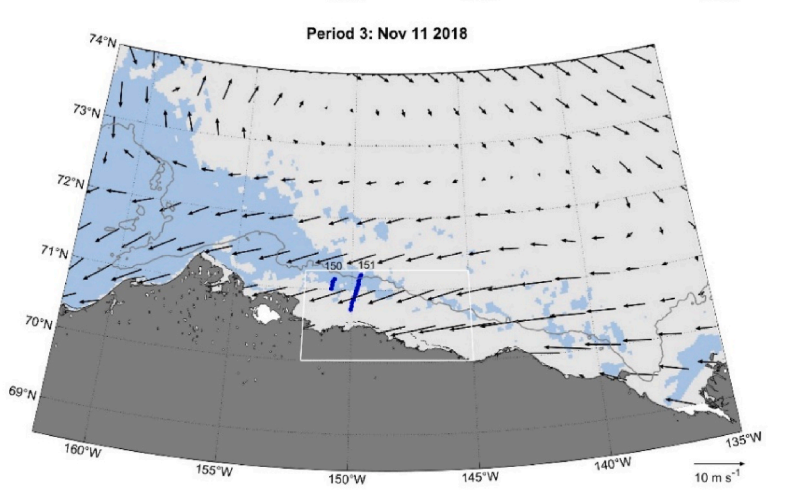


Fig. 3. Snapshots showing regions where polynyas were present (ice concentration <80%, light blue shading). (a) 1 Nov, during event #1. (b) 7 Nov, during event #2. (c) 12 Nov during event #3. The light grey shading corresponds to ice concentration >80%, and the vectors show the mean winds over the 24-hr period. The hydrographic stations occupied during or just following each of the events are displayed as blue dots, labeled by longitude. The 60-m isobath shows the shelf-edge (grey contour). The white box shows the area where ice concentrations are averaged and presented in Fig. 11.





mainly on the innermost shelf, inshore of the hydrographic stations. During period 2, corresponding to the strongest easterly winds, polynyas were present across the full width of the shelf. In period 3, when the ice was generally more concentrated, the polynya activity was mainly to the west of the study region, although polynyas were scattered along the edge of the shelf.

4.2. Hydrographic observations

We now present a subset of the hydrographic and velocity data obtained on the cruise that is relevant to the chemical results presented below. Fig. 4 shows vertical sections of temperature, density, absolute geostrophic velocity, and beam transmission for three of the transects: section 148 which was occupied after period 1; section 147 which was occupied at the end of period 2; and section 150 which was occupied near the end of period 3 (Fig. 3). In this study we define water colder than $-1.6\,^{\circ}$ C as WW, consistent with previous studies (e.g. Pacini et al., 2019; Pickart et al., 2016).

On section 148 there is WW throughout the water column at the two inner-most stations on the shelf (Fig. 4a). This is consistent with an extended polynya along the inner-shelf during period 1 (Fig. 3a) that likely resulted in the formation of this water. Beam transmission was lower at the two inner-most stations compared to the outer shelf (75–80% and 90–95%, respectively) indicative of high particle concentrations and substantial sediment resuspension. Phytoplankton blooms are unlikely during November due to light limitation (Pabi et al., 2008), so we rule out primary production as the main cause of high particle loads. The circulation was such that the eastward-flowing shelfbreak jet was re-established following period 1, and there was eastward flow on the shelf (even though the first event was brief, it was able to reverse the shelfbreak jet, not shown).

During period 2, WW was present over much of the shelf on section

147 (the first 8 stations, Fig. 4b). Particle concentrations were still highest at the inner-most stations on the shelf, coincident with the coldest WW, but lower than period 1. This section was done after the period of strongest easterly winds, which likely induced upwelling and reversed the shelfbreak jet. One sees evidence of the upwelling by the presence of the warm, dense near-bottom layer extending roughly 30 km inshore of the shelfbreak. The flow on the shelf was still directed to the west in response to the previous easterly winds, but in the vicinity of the shelfbreak the westward flow was confined to the upper part of the water column (Fig. 4b). Below 25m there was eastward flow at the shelfbreak, intensifying with depth. This is the so-called "rebound jet" that regularly spins up at the end of an upwelling event (Li et al., 2020; Pickart et al., 2011), due to the disparity in the barotropic and baroclinic shelf wave speeds following the cessation of the easterly winds (Pickart et al., 2011).

Section 150 was occupied near the end of the period 3 easterly winds. These winds were substantially weaker than the period 2 easterly winds (Fig. 3a), and the hydrographic sections show no evidence of upwelling inshore of the shelfbreak (Fig. 4c). This is not to say that upwelling did not take place, but the response of the water column was likely weak due to the relatively light winds. WW again occupied most of the shelf (the first 10 stations), but, in contrast to period 2, it was present throughout the water column. The region of cold WW (<-1.65 $^{\circ}$ C) also extended farther offshore. The isolated region of this cold WW at stations 173 and 174 coincided with the polynya at the shelf edge during period 3 (Fig. 3c). Beam transmission was again lower on the inner shelf, with extremely low values of 20-30% at the inner shelf stations where the coldest WW was found, indicating very high particle concentrations (Fig. 4c). The absolute geostrophic velocity shows westward flow across the entire section, with surface-intensified flow at the shelfbreak (Fig. 4c). In this case the rebound jet had not yet begun to appear since the winds were still out of the east.

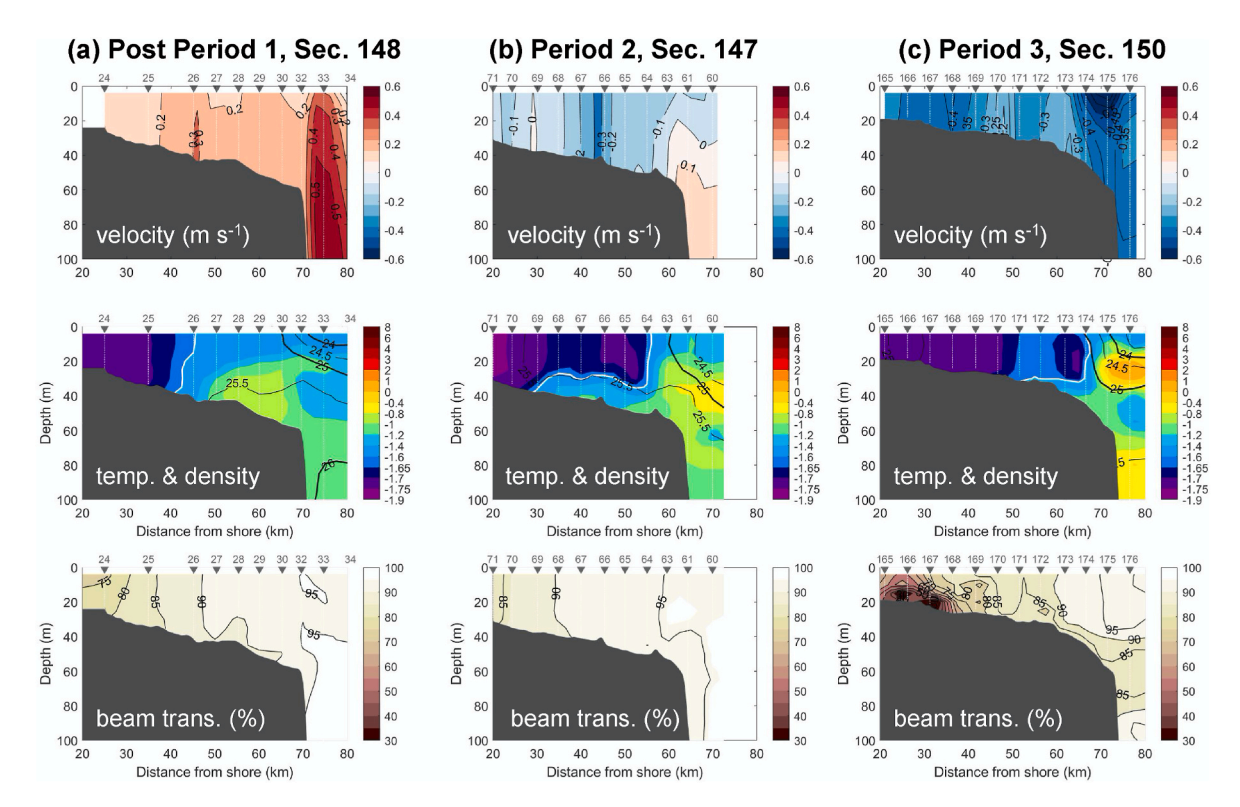


Fig. 4. Water column data for a subset of the transects. (column a) Post Period 1, section148; (column b) Period 2, section 147; (column c) Period 3, section 150. Top row: vertical sections of absolute geostrophic velocity (m s $^{-1}$), where positive velocities are to the east; Middle row: vertical sections of temperature (color, $^{\circ}$ C) overlain by density (black contours, kg m $^{-3}$). The white contour is the -1.6 $^{\circ}$ C isotherm, which delimits the WW; Bottom row: vertical sections of beam transmission (%). The small white dots indicate the CTD data points, and the station numbers are listed along the top above the dark grey triangles. The bottom data are from *Healy's* echosounder.

4.3. Radium isotopes & nutrients

Radium-228 and the ²²⁸Ra/²²⁶Ra activity ratio (AR) were both higher in shelf bottom waters than over the slope subsequent to period 1 (Fig. 5a and b). 228 Ra activities averaged 9.5 \pm 0.9 and 7.9 \pm 0.5 dpm 100 L⁻¹ on the shelf and on the slope, respectively. The ²²⁸Ra/²²⁶Ra AR was 0.79 ± 0.04 and 0.68 ± 0.05 on the shelf and on the slope, respectively. In surface waters, ²²⁸Ra activities and the ²²⁸Ra/²²⁶Ra AR were similar on the shelf and over the slope, with values of 8.2 \pm 0.3 dpm 100 L^{-1} and 0.71 \pm 0.05, respectively. During period 2, we observed that 228 Ra in shelf bottom waters was 8.6 ± 0.5 dpm $100 L^{-1}$, similar to the end of period 1. By period 3, ²²⁸Ra in bottom waters increased to 10.7 ± 0.8 dpm $100~L^{-1}.$ The $^{228}\mbox{Ra}/^{226}\mbox{Ra}$ ratio on the shelf decreased from 0.79 \pm 0.04 to 0.69 \pm 0.04 from the end of period 1 to period 2, and then increased to 0.82 \pm 0.07, with a maximum value of 0.91 by period 3. In surface waters on the central Beaufort shelf, ²²⁸Ra increased from 8.2 \pm 0.3 dpm 100 L^{-1} to 10.3 \pm 0.5 dpm 100 L^{-1} from post-period 1 to period 3. Similarly, the surface ²²⁸Ra/²²⁶Ra AR increased from 0.71 \pm 0.05 to 0.80 \pm 0.04. The increase in surface water activities caused an increase in the surface to bottom water ratios of ²²⁸Ra and ²²⁸Ra/²²⁶Ra AR (Fig. 5f). The observed ²²⁸Ra activities during all periods were within the range of historical samples from the late 1990s and early 2000s (Kadko et al., 2008; Kadko and Muench, 2005;

Kipp et al., 2019; Smith et al., 2003; Trimble et al., 2004), and higher than the 228 Ra activities measured to the east during period 2 of this study (Fig. 6). With the exception of the 1995 samples from the Canadian Beaufort shelf, all of the historical samples were collected slightly to the west of our study region. Both 228 Ra and 228 Ra/ 226 Ra were lower by a factor of \sim 2 compared with the Chukchi Sea Ra isotope data of Vieira et al. (2019). We attribute this to two main factors: (1) the shelf in this region is much wider compared to the Beaufort Shelf, and with prevailing currents that are cross shelf this allows for more accumulation of Ra isotopes from SWI; and (2) the strongest benthic inputs of Ra isotopes are during winter when WW formation and associated water column convection is at its highest (Kipp et al., 2020).

Short-lived radium isotopes were also measured on the cruise. For both $^{224}\rm{Ra}_{ex}$ and $^{223}\rm{Ra}_{ex}$, activities were generally higher at depth than in surface waters, with the exception of one $^{223}\rm{Ra}_{ex}$ sample in period 3 (Fig. 5c and d). Following period 1, when we sampled both on the shelf and over the slope, we observed that $^{224}\rm{Ra}_{ex}$ at depth was higher on the shelf, at 5–7 dpm 100 \rm{L}^{-1} , compared to slope activities of 3.8 dpm 100 \rm{L}^{-1} . $^{223}\rm{Ra}_{ex}$ was also higher in shelf bottom waters than along the same density surfaces in the basin, with activities of 0.22 and 0.10 dpm 100 \rm{L}^{-1} , respectively. The $^{224}\rm{Ra}_{ex}/^{223}\rm{Ra}_{ex}$ AR was approximately 20–25 on the shelf after period 1 (Fig. 5e). During period 2, we observed significantly higher $^{224}\rm{Ra}_{ex}$ in bottom waters (4.5 dpm 100 \rm{L}^{-1} at 20 km from

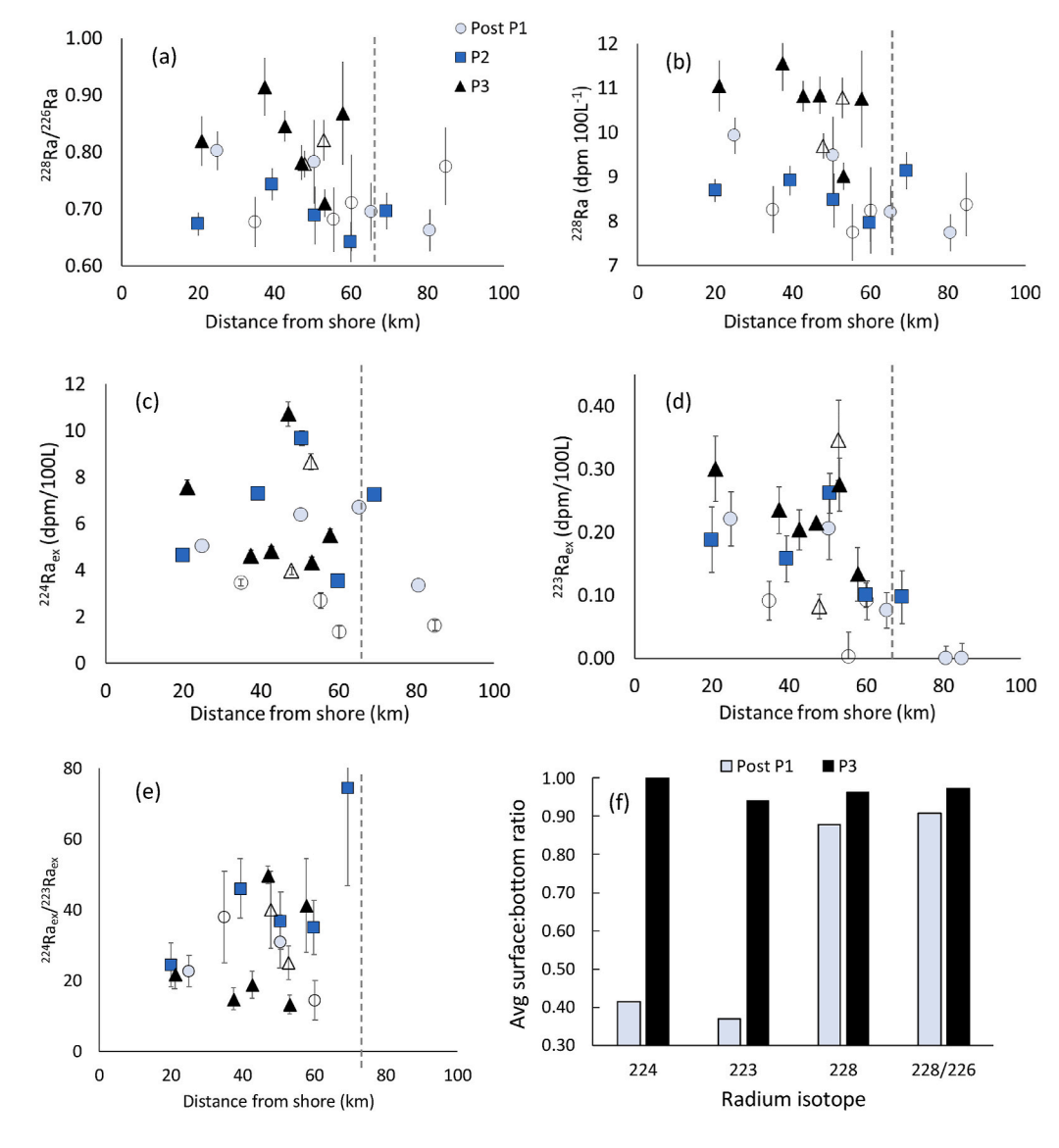


Fig. 5. 228 Ra/ 226 Ra (a), 228 Ra (b), 224 Ra $_{\rm ex}$ (c), 223 Ra $_{\rm ex}$ (d), 224 Ra $_{\rm ex}$ / 223 Ra $_{\rm ex}$ (e) and the average surface to bottom water ratio of each radium isotope (f) on the Beaufort shelf and slope. Light blue circles, blue squares and black triangles represent sampling during post-period 1, period 2 and period 3 (Nov 2–3, Nov 7, Nov 12–13), respectively. Filled symbols are bottom water samples. Open symbols are surface samples. The dashed grey line in (a–e) denotes the location of the shelfbreak. Samples with undetectable 223 Ra $_{\rm ex}$ are excluded from the 224 Ra $_{\rm ex}$ / 223 Ra $_{\rm ex}$ panel (e).

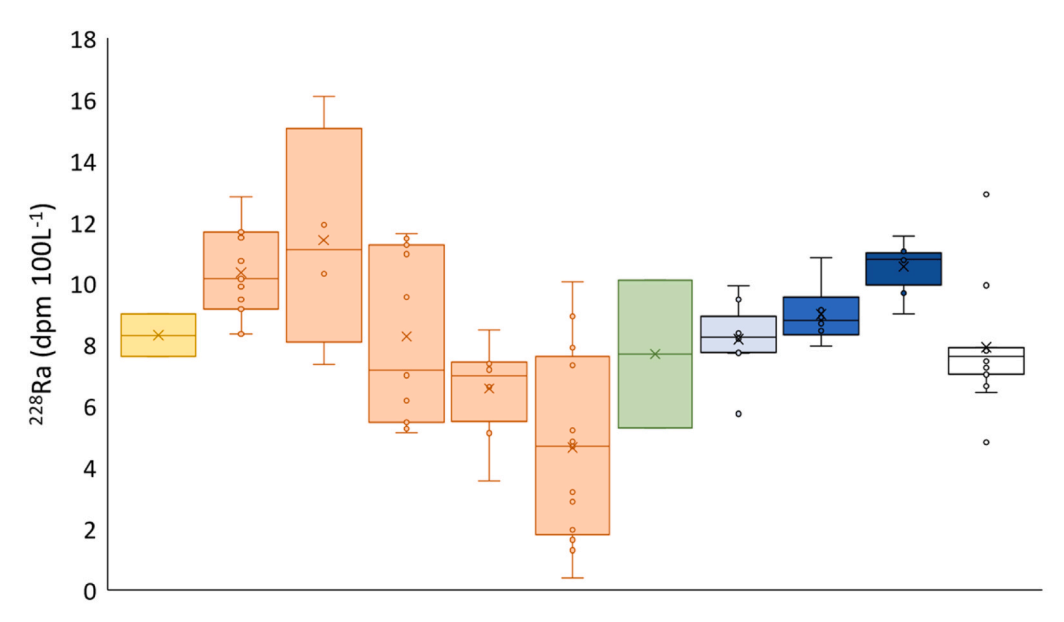


Fig. 6. Samples from this study compared to previous studies near the Alaskan and Canadian Beaufort Shelves. Historical samples are limited to 69-72°N and depths of 0-75 m for the closest comparison to this study (Kadko et al., 2008; Kadko and Muench, 2005; Kipp et al., 2019; Smith et al., 2003; Trimble et al., 2004). Historical samples are colored by season (yellow = spring, orange = summer, green = autumn). Post Period 1 (Nov 2-3), Period 2 (Nov 7), and Period 3 (Nov 12-13) are colored in light, medium and dark blue, respectively. Samples from the Eastern Beaufort shelf (east of ~152°W) collected during Period 2 of this study are shown in white.

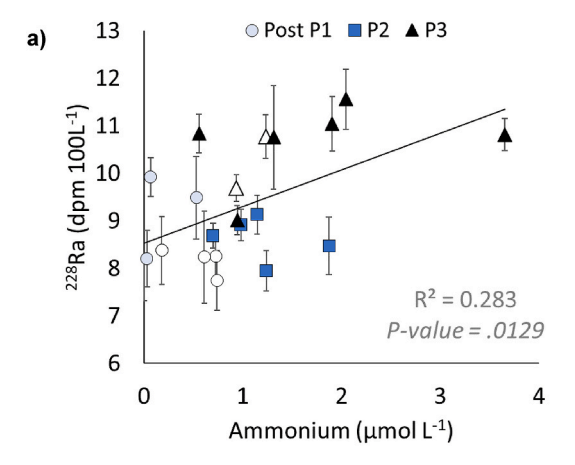
May-02 Aug-95 Aug-00 Aug-02 Aug-04 Sep-04 Oct-98 Post-P1 P2 P3 E.Beaufort

shore to 10 dpm 100 L^{-1} at 50 km from shore) and approximately equivalent activities of $^{223}{\rm Ra_{\rm ex}}$ (0.17–0.27 dpm 100 L^{-1}), with the highest activities at 50 km from shore. During period 3, $^{224}{\rm Ra_{\rm ex}}$ was 8 dpm 100 L^{-1} at 20 km from shore, and $\sim\!4.5$ dpm 100 L^{-1} on the outer shelf. One sample at 50 km from shore had $^{224}{\rm Ra_{\rm ex}}$ activities of 11 dpm 100 L^{-1} . $^{223}{\rm Ra_{\rm ex}}$ in bottom waters increased to 0.21–0.31 dpm 100 L^{-1} by period 3. The difference between surface and bottom water activities of $^{224}{\rm Ra}$ and $^{223}{\rm Ra}$ decreased from post period 1 to period 3, reflected in the strong increase in the surface-to-bottom water ratio of the isotopes (Fig. 5f). The $^{224}{\rm Ra_{\rm ex}}/^{223}{\rm Ra_{\rm ex}}$ AR was highest at the shelf edge during period 2 (Fig. 5e).

Radium isotope activities were compared to ammonium concentrations in the water column during periods 1-3 (Fig. 7). Statistically significant (95% confidence level, *P-value* < 0.05) relationships were found for ²²⁸Ra and ²²³Ra_{ex}. There was not a statistically significant relationship for 226 Ra or 224 Ra $_{\rm ex}$ with ammonium. Ammonium concentrations in shelf bottom waters consistently increased from post period 1 to period 3 (Figs. 7 and 8), and were consistent with near-bottom values observed in this general vicinity during the SBI project (Codispoti et al., 2005, 2009). In post period 1, NH_4^+ concentrations were ~ 0 –0.5 μ M. Surface waters were similarly depleted in NH₄⁺. During period 2, concentrations increased to 0.8-2.0 µM, with the highest concentration at 45 km from shore. Surface waters were still depleted, with the exception of one surface sample with a concentration of 1.4 μM at 30 km from shore. During period 3, NH_4^+ concentrations were $\sim 2 \mu M$ at a distance of 20–30 km from shore, nearly 4 μM at ~40 km from shore, coinciding with very high particle concentrations (Fig. 4), and approximately $0.6-1.3 \,\mu\text{M}$ at 40 km from shore to the shelfbreak (Fig. 8). Surface waters were on average higher in NH₄⁺ during period 3 compared to the previous periods.

4.4. Sediments

Bulk surface sediments were collected using a Van Veen grab along most transects and analyzed for radium isotopes. In general, sediments were a mix of mud, sand and gravel with a mean coarse (>63 μm) fraction of 28% (Gemery et al., 2021). The relatively high coarse fraction is consistent with the composition of sediment that is transported via ice rafting over this shelf as previously reported by Barnes et al. (1982). The sediment surface-available $^{224} Ra/^{223} Ra$ ratio was within analytical error along the transects from the inner to outer shelf (Fig. 9a). The ratios



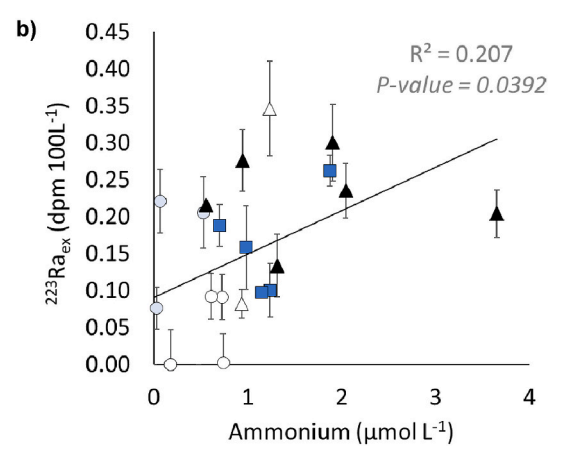


Fig. 7. (a) 228 Ra and (b) 223 Ra $_{\rm ex}$ plotted with respect to ammonium concentrations. Post Period 1 (Nov 2–3), Period 2 (Nov 7), and Period 3 (Nov 12–13) are shown by circles, squares and triangles, respectively. Filled symbols are bottom waters and unfilled symbols are surface waters. The regression parameters are shown in grey text for the best linear fit to all of the data (black line).

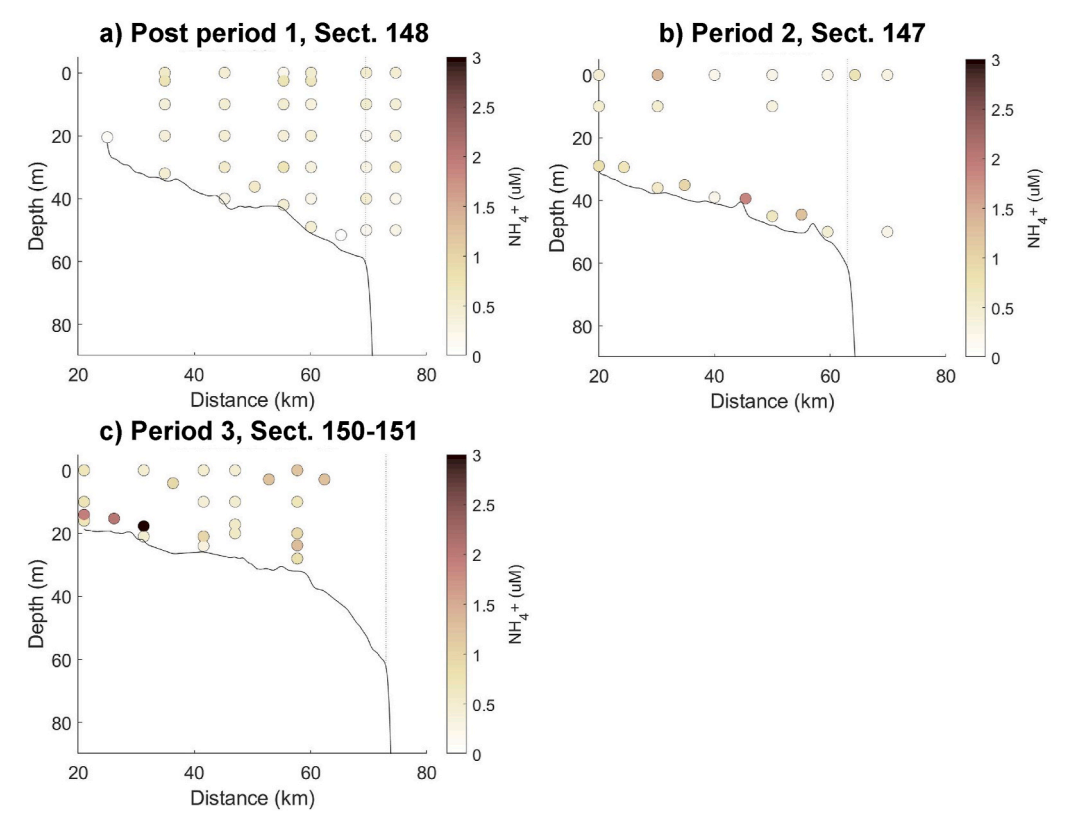


Fig. 8. Cross-sectional distributions of ammonium concentration during Post-period 1 (A, Nov 2–3), Period 2 (B, Nov 7), and Period 3 (C, Nov 12–13). The black line shows the bathymetry. The grey dashed line marks the approximate shelf edge.

ranged from 19 to 47, with little variation beyond analytical uncertainties (Fig. 9a).

Activities of 226 Ra in bulk surface sediments were 1.2–2 dpm g $^{-1}$ (Fig. 9b), with a decreasing trend from inner to outer shelf along Section 152 and Section 140, and increasing from inner to outer shelf along sections 148 and 144. 228 Ra activities in bulk sediment were 1–2.6 dpm g $^{-1}$ (Fig. 9c). Similar cross-shelf trends in 228 Ra were observed as compared to 226 Ra. The 228 Ra/ 226 Ra AR was 0.8–1.4, and on average higher in the eastern transects (140–144°W) than in the western transects (148–152°W) (Fig. 9d). The eastern transects are likely influenced by the Mackenzie River (Goñi et al., 2013); however, the focus of this paper is in the region farther to the west at longitudes 147–151°W.

4.5. Radium ages

Since sediments are the main source of short-lived radium isotopes in the water column, we can calculate the age of the water, *t*, or time since SWI occurred, using the following equation (Moore, 2000):

[224 Ra/ 223 Ra]_{obs} is the observed water column ratio, [224 Ra/ 223 Ra]_i is the initial AR found in surface sediments (from Fig. 9), and λ_{224} and λ_{223} are the decay constants, equal to 0.189 and 0.061 d⁻¹, respectively. In this model we assume that (1) bottom sediment porewaters are in equilibrium with surfaces of the sediments, (2) bottom sediments are the main source of 223 Ra_{ex} and 224 Ra_{ex} in the water column, and (3) 223 Ra and 224 Ra are desorbed in roughly equal proportion to their sediment source. Samples with greater than 50% relative error were excluded from the calculation. From post-period 1 to period 2, ages decreased from 2.3-5.4 days to 0.9–4.1 days (Fig. 10). Ages of bottom water on the shelf then increased to 5.0–7.9 days from period 2 to 3, with the exception of one very young sample at ~60 km from shore that had an

age of \sim 0.1 days.

5. Discussion

5.1. Tracers of sediment-water interaction

During the cruise, we occupied transects across the Beaufort shelf during three periods in November 2018 with contrasting physical conditions as presented above: 1) following a brief and moderate upwelling storm with polynyas present mainly along the coast; 2) at the end of a strong upwelling storm associated with extensive polynya presence across the shelf; and 3) near the end of a weak upwelling storm with higher ice concentrations and polynyas only present at the outer shelf. Below we discuss the physical response of the water column to these drivers and the expected impact on SWI.

Radium isotopes can be used as tracers of SWI on continental shelves. Most surface sediments collected on the cruise had $^{228}\text{Ra}/^{226}\text{Ra}$ ARs greater than 1 (Fig. 9). Typically, waters on the Beaufort shelf and in the Canada Basin have $^{228}\text{Ra}/^{226}\text{Ra}$ ratios $\leq \! 1$ (Kadko et al., 2008; Kadko and Muench, 2005; Smith et al., 2003; Trimble et al., 2004), so increases of water column ARs towards 1 or more indicate influence from sediments. SWI causes increases in ^{228}Ra , and has been well characterized as a tracer on the Chukchi shelf (Kipp et al., 2020; Vieira et al., 2019).

The short-lived radium isotopes ²²⁴Ra and ²²³Ra have a similar sediment source, but their distribution is influenced by decay on time-scales of days to weeks (Colbert and Hammond, 2008; Hancock et al., 2000; Moore et al., 2006). Ammonium produced in sediments can also be released simultaneously into coastal waters due to SWI (Bianchi et al., 1997; Brown et al., 2015; Moore et al., 2019). Sediment-derived ammonium is similarly short-lived to ²²³Ra and ²²⁴Ra (Cai et al., 2015), though its loss is due to biological processes in the water column (Lee et al., 2010; Tremblay et al., 2006), including oxidation to nitrate, which has been shown to be most intense in shelf environments at depth

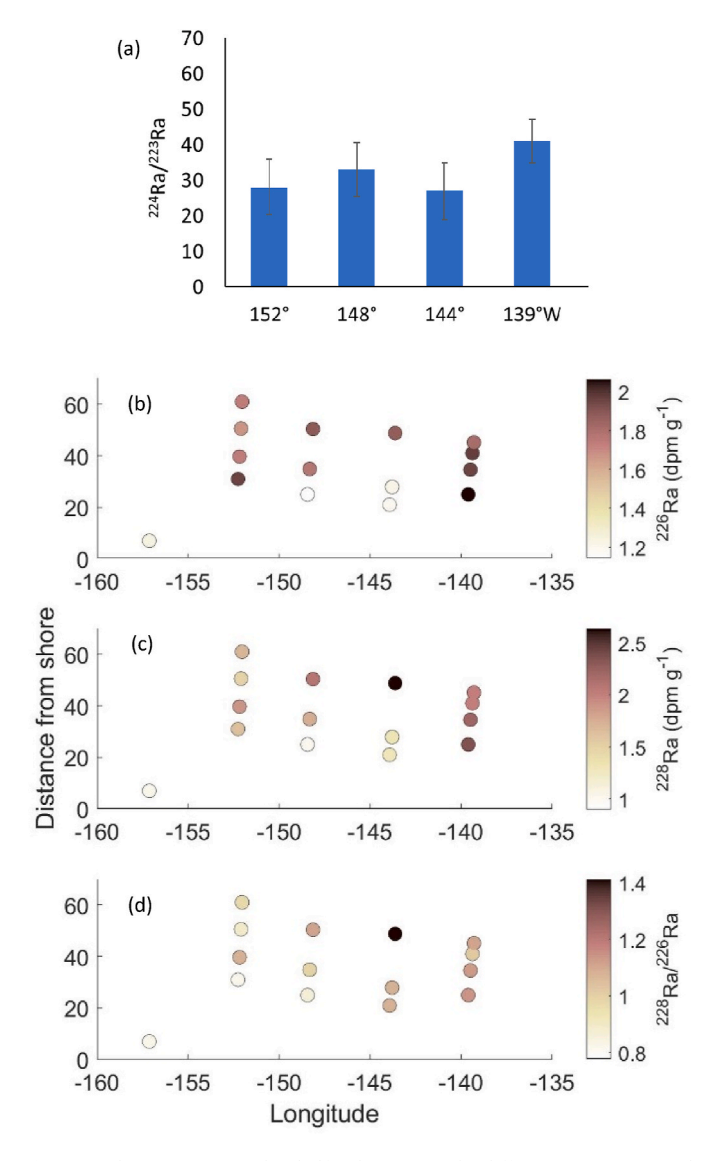


Fig. 9. Radium isotopes in the shelf sediments on the different transects. Panel (a) shows surface available activity ratios of 224 Ra/ 223 Ra. Panels b–d are bulk sediment radium activities measured via gamma spectrometry.

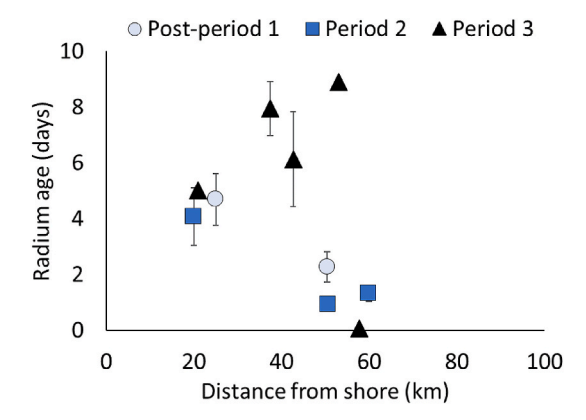


Fig. 10. Radium ages of bottom waters (time since sediment-water interaction) on the Beaufort shelf. Ages were calculated using bottom water 224 Ra_{ex}/ 223 Ra_{ex} activity ratios. Post Period 1 (Nov 2–3), Period 2 (Nov 7), and Period 3 (Nov 12–13) are shown by circles, squares and triangles, respectively.

under low light conditions (Heiss and Fulweiler, 2016) similar to those that were encountered during this cruise. Together, these tracers have low backgrounds in the water column, which makes them more sensitive than ²²⁸Ra or ²²⁶Ra to recent SWI (Ardyna et al., 2017; Bianchi et al., 1997; Charette et al., 2008; Ku and Luo, 2008; Moore, 2000). In general, ²²⁸Ra is useful as a tracer of the total amount of SWI, while ²²⁴Ra and ²²³Ra provide complementary information about the timing of SWI on the order of days.

Regarding the possible mechanisms of SWI in this environment, we know from analysis of samples collected on our own cruise (Gemery et al., 2021), as well as from historical studies, that the Beaufort shelf sediments have a substantial coarse fraction with the exception of those at the mouth of the Mackenzie River delta (well to the east of our focus area) (Barnes et al., 1982; Goñi et al., 2013). This would minimize the critical shear stress at which erosion of bottom sediment is initiated, yet allow WW to penetrate into the sediments due to their higher permeability. This of course does not exclude the possibility that physical reworking of sediments is a contributing mechanism for SWI (e.g. Wei et al., 2021); however, as we argue below, the timing of Ra isotope and ammonium increases in the near bottom environment favors WW as an important added driving force of SWI.

5.2. Post-period 1 (nov 2-3, 2018): inner shelf WW formation

The typical flow on the outer Alaskan Beaufort shelf and upper slope is towards the east, associated with the Beaufort shelfbreak jet (Nikolopoulos et al., 2009; Pickart, 2004). On the mid-shelf there have been no long-term mooring measurements, although data from a year-long array (2008-9) near 150°W showed westward mean flow on the mid and inner shelf (Weingartner et al., 2017). Wind events, such as storms with strong easterly winds that are common in autumn, can reverse the shelfbreak jet and intensify the westward flow on the mid-shelf (Lin et al., 2019). These events commonly lead to upwelling of water from the slope onto the shelf (Pickart et al., 2009, 2011; Pickart et al., 2013a; Lin et al., 2019). Prior to the occupation of section 148, there was a brief storm (i.e., Period 1), lasting about 1.5 days (Figs. 3 and 11), with conditions that would favor upwelling. However, there is no compelling evidence that significant upwelling took place (Fig. 4a), other than the upward-sloping 25.5 kg m⁻³ isopycnal from the slope to the outer shelf. According to the absolute geostrophic velocity (Fig. 4a), the shelfbreak jet was flowing to the east, and the flow on the shelf was directed eastward as well. The average sea ice concentrations in the study area were the lowest of the three periods, ~60-70% (Fig. 11), and large polynyas were present at this time along the inner shelf (Fig. 3a). Notably, many of the polynyas and leads encountered during the cruise were in the process of freezing over, which results in brine-driven convective overturning and water mass transformation. This is consistent with the WW observed at the two shoreward-most stations on section 148.

During this period, ²²⁸Ra and the ²²⁸Ra/²²⁶Ra AR in bottom waters were slightly elevated at the inner shelf compared to the outer shelf (Fig. 5a and b), coinciding with the presence and lack of WW, respectively. In surface waters, all four radium isotopes were at lower activities than in bottom waters. The elevation of ²²⁸Ra at the inner shelf and presence of WW also coincided with high particle concentrations, suggestive of bottom sediments having been recently resuspended. This makes sense in that vertical velocities during convective overturning can be quite large (nearly 10 cm/s, Lilly et al., 1999), causing the dense water to interact strongly with the sediments. As documented in Pacini et al. (2019), the convected water within refreezing leads on the Chukchi shelf can quickly reach the bottom, and the Beaufort shelf is similarly shallow. We also note that earlier studies of WW on the Chukchi shelf revealed a very high correlation between the salinity of the dense water and its nitrate content (Arrigo et al., 2008; Pacini et al., 2019). The enhanced salinity is due to brine-rejection, and the source of the nutrients is the sediments (Vieira et al., 2019). Taken together, it is likely that

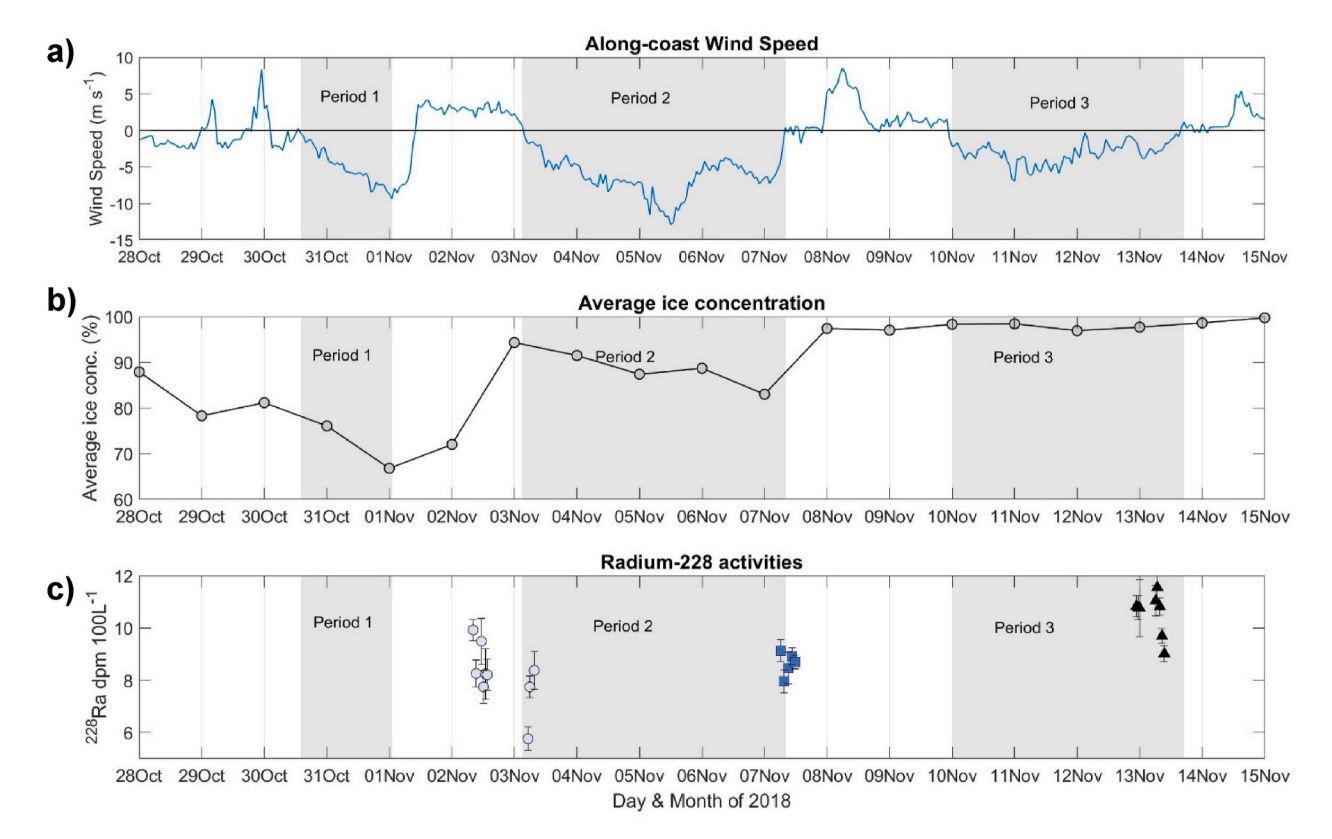


Fig. 11. Wind speeds, ice concentration and radium-228 activities. (a) Alongcoast wind speed from the Barrow Atmospheric Baseline Observatory. (b) Average sea ice concentration calculated using AMSR-2 data on the central Beaufort shelf (70–71.25°N, 145–152°W, marked on Fig. 6). (c) ²²⁸Ra activities measured on the central Beaufort shelf after period 1 (circles), at the end of period 2 (squares), and near the end of period 3 (triangles).

brine-driven convection was driving SWI at these inshore stations. The elevation of 228 Ra is within the range of previous studies, but lower than subsequent sampling periods during this study (Figs. 5 and 11) when WW formation was more prevalent across the entire study domain. It should be noted as well that the shear flow near the bottom can also play a role in the SWI, particularly on the outer shelf where the WW was not formed and the horizontal flow was stronger (Fig. 4a).

5.3. Period 2 (nov 3-7, 2018): storm 2 and mid-shelf WW formation

During Period 2, there were strong easterly winds (Fig. 11) that drove upwelling onto the Beaufort shelf (Fig. 4b). Here we focus on the central Beaufort shelf at Section 147 sampled on Nov 7 at the end of Period 2 (Fig. 2), and exclude sections 139 and 144 that were significantly farther east (Fig. 1b). There is little doubt that the shelfbreak jet was reversed due to this strong easterly wind event (greater than 95% of storms of this magnitude reverse the shelfbreak jet and cause upwelling; Schulze and Pickart, 2012). As the winds relaxed and the section was occupied, the rebound jet appeared and the shelfbreak jet was in the process of returning to its normal condition of eastward flow. Water from the slope was present in a thin bottom layer extending well onto the shelf (Fig. 4b). Polynyas developed across much of the shelf (Fig. 3), consistent with the sustained easterly winds that opened up leads in the ice. This is reflected in the decrease in mean sea ice concentration during the event (Fig. 11). The re-freezing of the polynyas likely drove convection and formation of WW, consistent with the observations of WW over most of the shelf (Fig. 4b).

There are two potential interpretations of the warm dense bottom layer on the shelf: 1) WW-driven convection occurred after upwelling commenced and did not penetrate the bottom waters, and 2) WW-driven convection occurred first, followed by the upwelling of slope water. Brine-driven overturning on the Chukchi shelf can reach the bottom on

timescales of minutes to hours (Pacini et al., 2019), and the central Beaufort shelf is roughly the same depth as the Chukchi shelf, so it is likely that convectively formed WW did reach the bottom prior to the upwelling, resulting in active SWI at the central shelf stations. Further, the onset of upwelling typically lags the onset of easterly winds by about 18 h (Pickart et al., 2009), so we suspect that scenario 2 is more likely. We therefore expect to see chemical signals of SWI on the central shelf.

From post-period 1 to period 2, we observed similar $^{228}\mathrm{Ra}/^{226}\mathrm{Ra}$ ARs and a slight increase in average ²²⁸Ra (Fig. 5a and b and 11), but saw a significant increase in ²²⁴Ra and ²²⁴Ra/²²³Ra in bottom waters (Fig. 5c, e), likely due to the difference in the sensitivity of these tracers to SWI in this region. Ammonium, also increased in surface waters at 30 km from shore and in several bottom water samples at 40-60 km from shore (Fig. 8). Radium age decreased from 2-3 days to 1-2 days (Fig. 10), due to ²²⁴Ra activities increasing by nearly 50% at this location (Fig. 5c), which overlaps with the location of increased NH₄⁺ concentrations (Fig. 8) and with the presence of WW (Fig. 4b). This suggests that refreezing in the polynyas likely caused strong enough vertical convection to reach the bottom and induce SWI, supporting the second scenario described above. Since this was also at the end of a strong storm event, we cannot rule out the influence of winds on vertical convection or shear flow near the bottom, especially since mobile sea ice can enhance the surface stress imparted to the water column (Martin et al., 2014; Pickart et al., 2011). The easterly winds also likely drove the opening of the polynyas, allowing for WW formation. Thus, the observed chemical response may be due to the combined drivers of wind and buoyancy.

5.4. Period 3 (nov 10-14): storm 3 and WW development

Section 150 was occupied near the end of period 3, corresponding to another period of easterly winds (Fig. 3). However, unlike the previous storm, the winds during this event barely reached the 4–5 m s⁻¹

threshold for upwelling, and while the shelfbreak jet was reversed, there was no indication of transport of slope waters onto the shelf. During period 3, highly concentrated sea ice covered most of the central Beaufort shelf (Fig. 11) except in the vicinity of the shelfbreak where there were numerous polynyas (Fig. 3). At the same time, the previously formed WW on the inner and central shelf should tend to progress offshore (Gawarkiewicz and Chapman, 1995), although this could be influenced by wind. Interestingly, we observed the presence of very cold (<-1.65 °C) WW at two of the stations near the shelfbreak (60–70 km from shore, Fig. 4c) in the very region of the polynyas (Fig. 3). The inner shelf WW coincided with highly turbid waters (Fig. 4c). This could be due to continued convection in this region, which began during period 1, or to the lateral advection of the very dense water as it flows along the bottom after convection (Gawarkiewicz and Chapman, 1995), both of which have the potential to resuspend sediments.

Across the shelf during period 3, we observed significant changes in both radium isotopes and ammonium. There were meaningful increases in the ²²⁸Ra/²²⁶Ra AR and ²²⁸Ra in both bottom and surface waters compared to the earlier periods (Fig. 5a and b). Increases in the surface to bottom water ratio of all radium isotopes is indicative of decreased stratification across the shelf where there was buoyancy-driven sediment resuspension and extensive WW formation (Fig. 4c). The comparable levels of radium isotopes near the bottom and surface also suggest that the role of the shear flow was not significant in this period, which would lead to larger isotope values in the bottom boundary layer. We note that the strong westward currents during this time would transport water from the east at 35-40 km d⁻¹, so in addition to local SWI, we might expect chemical signals to be influenced by shelf waters that originated in the eastern Beaufort. However, the lower ²²⁸Ra activities in the eastern Beaufort during this study and in 1995 compared to western Beaufort historical samples and samples from periods 1–3 (Fig. 6 and S4) suggest that typical summer and autumn shelf waters from the eastern Beaufort are depleted in radium isotopes. Therefore, the increase in ²²⁸Ra that we observe is likely due to recent and local SWI. We expect that ²²⁸Ra would increase further during the ice-covered months as polynyas form and cause continued SWI, as modeled in the Chukchi Sea by Kipp et al. (2020), until a new steady-state is reached where off-shelf mixing losses prevent further rise in concentration over the shelf.

During all study periods, ²²³Ra_{ex} and ²²⁸Ra were linearly correlated with ammonium concentrations, showing their shared sediment source (Fig. 7; Cai et al., 2015). Ammonium was highly enriched in bottom waters at 20–30 km from shore, especially in the nepheloid layer with extremely low beam transmission (Fig. 4c), and at elevated concentrations throughout the water column at 60 km from shore (Fig. 8), coinciding spatially with regions of WW (Fig. 4). The average NH₄⁺ concentrations on the mid-shelf (30–60 km from shore, full water column profiles) increased from 0.4 to 1.0 µM from post-period 1 to period 3 (Fig. 8). Combined, the long-lived isotopes and ammonium show strong evidence of SWI coinciding with WW developing over the two-week timeseries.

Increases of $^{228}\mathrm{Ra}$ with time provide evidence of increasing SWI due to WW formation, while short-lived radium isotopes provide details about the timing of the SWI event and speed of convection. From period 2 to 3 the radium age increased from 1-4 days to 5-9 days at the inner shelf where the coldest and most well-mixed WW was observed (Fig. 10). This suggests that the convection taking place around the time that section 147 was occupied on Nov 7 continued beyond Period 2, further enriching the long-lived radium isotopes and ammonium, but ceased before we returned to the area and occupied section 150 on Nov 12-13. Hence the short-lived radium isotopes that were released during the active convection had already decayed. The exception to this was at the station ~60 km from shore, where we observed the isolated region of WW beneath the region of polynyas (Fig. 4). Here the radium age was <1 day in bottom waters (Fig. 10), which indicates that the station was occupied very close to the time of active convection. This rapid, buoyancy-driven convection is consistent with overturning timescales of hours during WW formation in the Chukchi Sea (Pacini et al., 2019).

6. Conclusion

The data presented in this study are among the first to document the combined physical and chemical signals of winter water formation in the Beaufort Sea, made possible by repeat occupations of the central Beaufort shelf over a two-week time period in November 2018. In addition to year-round mooring observations (Itoh et al., 2012; Weingartner et al., 1998), late spring cruises (Pacini et al., 2019; Vieira et al., 2019), and modeling evidence (Kipp et al., 2020), this study highlights the patchiness of the ice formation process and its ability to stir dissolved constituents from sediment porewaters into the water column via brine-driven convective overturning, together with wind-driven processes, not only during autumn, but also throughout winter to early spring. It further suggests that these SWI events are episodic in nature, and that storms and the resulting mesoscale water column features can drive local exchange with the benthos. Future studies may be able to use these isotopes as tracers to monitor changes in the sedimentary sources of nutrients; however, they should include parallel measurements of changes in porewater nutrients and SWI tracers (e.g. Wei et al., 2021). Large inputs of ammonium were observed, which presumably occur throughout the winter and spring as leads in the ice allow for more ice formation (Reimnitz et al., 1994). The ammonium produced during winter water formation in ice covered months is likely converted to nitrate by nitrification (Shiozaki et al., 2019) which can feed spring blooms on the shelf (Tremblay et al., 2006). For this deeper shelf water that is transported offshore (e.g., in the halocline), ice cover and the depth of these SWI-derived nutrients may limit their ability to contribute to primary productivity (Codispoti et al., 2005, 2009).

Climate change is causing increases in primary production in the Arctic Ocean: in the early 2000s, areas of primary production increased due to decreases in sea ice and light limitation (Ardyna et al., 2014; Arrigo et al., 2008; Lewis et al., 2020). Since 2008, continued increases in primary production were driven largely by increases in biomass rather than open water area, likely due to an influx of new nutrients (Lewis et al., 2020). As the climate continues to warm, our study suggests that sediment-water exchange processes during winter water formation, will become a crucial source of nutrients that continues to support increases in productivity in the Arctic. Other drivers of sediment-water interaction, such as wind and potentially submarine groundwater discharge, which has not been well characterized in the Arctic (Lecher, 2017), are likely to increase over time (Rainville et al., 2011; Walvoord and Kurylyk, 2016). High temporal resolution of radium isotope measurements and nutrients via moorings or autonomous platforms could further elucidate the drivers of sediment-water interaction throughout the year and help quantify nutrient inputs that are driving increases in primary productivity (Lewis et al., 2020). Increases in total shelf inputs to the central Arctic have been observed for ²²⁸Ra and other trace elements and isotopes with sediment sources (Charette et al., 2020; Kipp et al., 2018; Rutgers van der Loeff et al., 2018), but disentangling the changes due to river inputs versus shelf processes, and the potential role of submarine groundwater discharge due to thawing permafrost (Charkin et al., 2017), can allow us to predict future changes in biogeochemical cycles in the Arctic as it continues to warm at an unprecedented rate.

Declaration of competing interest

The authors declare that they have no known competing financial interests or personal relationships that could have appeared to influence the work reported in this paper.

Acknowledgements

The authors would like to acknowledge the amazing work of Captain

Greg Tlapa and the crew of the USGCG Healy to sample in heavy ice during HLY 1803. The ship overcame repeated challenges to enable the cross-shelf transects to be completed. The authors acknowledge Joseph Tamborski for guidance and mentorship on sediment analyses, Paul Henderson for the nutrient analyses, Frank Bahr for the ADCP data processing, and Astrid Pacini for her assistance with MATLAB. We also thank Laura Gemery for providing grain size data on the box cores collected during HLY 1803. The manuscript greatly benefited from feedback provided by three anonymous reviewers, Associate Editor Yang, and Editor Fang. This work was funded by the Montrym Fund at the Massachusetts Institute of Technology, the Academic Programs Office at Woods Hole Oceanographic Institution, and the NSF Arctic GEOTRACES (OCE-1458305), Pacific GEOTRACES (OCE-1736277), and Arctic Observing Network (OPP-1733564; PLR-1504333) programs. Data not included in the manuscript are available for download at http://aon.whoi.edu/under cruise identifier HLY 1803.

References

- Aagaard, K., Coachman, L.K., Carmack, E., 1981. On the halocline of the Arctic Ocean. Deep Sea Res. Part A, Oceanographic Research Papers 28 (6), 529-545. https://doi. org/10.1016/0198-0149(81)90115-1.
- Ardyna, M., Babin, M., Gosselin, M., Devred, E., Rainville, L., Tremblay, J.É., 2014. Recent Arctic Ocean sea ice loss triggers novel fall phytoplankton blooms. Geophys. Res. Lett. 41 (17), 6207-6212. https://doi.org/10.1002/2014GL061047.
- Ardyna, M., Babin, M., Devred, E., Forest, A., Gosselin, M., Raimbault, P., Tremblay, J., 2017. Shelf-basin gradients shape ecological phytoplankton niches and community composition in the coastal Arctic Ocean (Beaufort Sea), Limnol, Oceanogr, 62 (5), 2113-2132, https://doi.org/10.1002/lno.10554.
- Arrigo, K.R., van Dijken, G., Pabi, S., 2008. Impact of a shrinking Arctic ice cover on marine primary production. Geophys. Res. Lett. 35 (19) https://doi.org/10.1029/ 2008GL035028
- Barnes, P.W., Reimnitz, E., Fox, D., 1982. Ice rafting of fine-grained sediment, a sorting and transport mechanism, Beaufort Sea, Alaska. J. Sediment. Petrol. 52 (2), 493–502. Beitsch, A., Jungclaus, J.H., Zanchettin, D., 2014. Patterns of decadal-scale Arctic
- warming events in simulated climate. Clim. Dynam. 43 (7), 1773-1789.
- Bianchi, M., Feliatra, F., Tréguer, P., Vincendeau, M.A., Morvan, J., 1997. Nitrification rates, ammonium and nitrate distribution in upper layers of the water column and in sediments of the Indian sector of the Southern Ocean. Deep-Sea Res. Part II Top. Stud. Oceanogr. 44 (5), 1017-1032. https://doi.org/10.1016/S0967-0645(96)
- Brown, Z.W., Casciotti, K.L., Pickart, R.S., Swift, J.H., Arrigo, K.R., 2015. Aspects of the marine nitrogen cycle of the Chukchi Sea shelf and Canada Basin. Deep-Sea Res. Part II Top. Stud. Oceanogr. 118, 73-87. https://doi.org/10.1016/j.dsr2.2015.02.009.
- Bruland, K.W., Lohan, M.C., 2003. Controls of trace metals in seawater. Treatise on Geochmistry 6, 23-47.
- Burt, W.J., Thomas, H., Pätsch, J., Omar, A.M., Schrum, C., Daewel, U., Brenner, H., de Baar, H.J.W., 2014. Radium isotopes as a tracer of sediment-water column exchange in the North Sea. Global Biogeochem. Cycles 28 (8), 786-804. https://doi.org 10 1002/2014GB004825
- Cai, P., Shi, X., Moore, W.S., Dai, M., 2012. Measurement of 224Ra:228Th disequilibrium in coastal sediments using a delayed coincidence counter. Mar. Chem. 138-139, 1-6. https://doi.org/10.1016/j.marchem.2012.05.004.
- Cai, P., Shi, X., Moore, W.S., Peng, S., Wang, G., Dai, M., 2014. ²²⁴Ra: ²²⁸Th disequilibrium in coastal sediments: implications for solute transfer across the sediment-water interface. Geochem. Cosmochim. Acta 125, 68-84. https://doi.org/ 10.1016/j.gca.2013.09.029.
- Cai, P., Shi, X., Hong, Q., Li, Q., Liu, L., Guo, X., Dai, M., 2015. Using 224Ra/228Th disequilibrium to quantify benthic fluxes of dissolved inorganic carbon and nutrients into the Pearl River Estuary. Geochem. Cosmochim. Acta 170, 188-203.
- Carmack, E.C., Chapman, D.C., 2003. Wind-driven shelf/basin exchange on an Arctic shelf: the joint roles of ice cover extent and shelf-break bathymetry. Geophys. Res. Lett. 30 (14) https://doi.org/10.1029/2003GL017526.
- Charette, M.A., Moore, W.S., Burnett, W.C., 2008. Uranium-and thorium-series nuclides as tracers of submarine groundwater discharge. Radioact. Environ. 13, 155–191.
- Charette, M.A., Kipp, L.E., Jensen, L.T., Dabrowski, J.S., Whitmore, L.M., Fitzsimmons, J. N., et al., 2020. The transpolar drift as a source of riverine and shelf-derived trace elements to the central Arctic Ocean. J. Geophys. Res.: Oceans (125), e2019JC015920. https://doi.org/10.1029/2019jc015920.
- Charkin, A.N., Rutgers van der Loeff, M., Shakhova, N.E., Gustafsson, Ö., Dudarev, O.V., Cherepnev, M.S., Salyuk, A.N., Koshurnikov, A.V., Spivak, E.A., Gunar, A.Y., Ruban, A.S., Semiletov, I.P., 2017. Discovery and characterization of submarine groundwater discharge in the Siberian Arctic seas: a case study in the Buor-Khaya Gulf, Laptev Sea. Cryosphere 11 (5), 2305-2327. https://doi.org/10.5194/tc-11-
- Cid, A.P., Nakatsuka, S., Sohrin, Y., 2012. Stoichiometry among bioactive trace metals in the Chukchi and Beaufort Seas. J. Oceanogr. 68 (6), 985-1001. https://doi.org/ 10.1007/s10872-012-0150-8.

- Codispoti, L.A., Flagg, C., Kelly, V., Swift, J.H., 2005. Hydrographic conditions during the 2002 SBI process experiments. Deep Sea Res. Part II Top. Stud. Oceanogr. 52 (24-26), 3199-3226.
- Codispoti, L.A., Flagg, C.N., Swift, J.H., 2009. Hydrographic conditions during the 2004 SBI process experiments. Deep Sea Res. Part II Top. Stud. Oceanogr. 56 (17), 1144-1163.
- Colbert, S.L., Hammond, D.E., 2008. Shoreline and seafloor fluxes of water and shortlived Ra isotopes to surface water of San Pedro Bay, CA. Mar. Chem. 108 (1-2), 1-17. https://doi.org/10.1016/j.marchem.2007.09.004
- Corlett, W.B., Pickart, R.S., 2017. The Chukchi slope current. Prog. Oceanogr. 153, 50-56. https://doi.org/10.1016/j.pocean.2017.04.005.
- Cota, G.F., Pomeroy, L.R., Harrison, W.G., Jones, E.P., Peters, F., Sheldon, W.M., Weingartner, T.R., 1996. Nutrients, primary production and microbial heterotrophy in the southeastern Chukchi Sea: Arctic summer nutrient depletion and heterotrophy. Mar. Ecol. Prog. Ser. 135 (1-3), 247-258. https://doi.org/10.3354/
- Foukal, N.P., Pickart, R.S., Moore, G.W.K., Lin, P., 2019. Shelfbreak downwelling in the alaskan Beaufort sea. J. Geophys. Res.: Oceans 124 (10), 7201-7225. https://doi.
- Gawarkiewicz, G., Chapman, D.C., 1995. A numerical study of dense water formation and transport on a shallow, sloping continental shelf. J. Geophys. Res. 100 (C3), 4489-4507. https://doi.org/10.1029/94JC01742.
- Gemery, L., Cronin, T.M., Cooper, L.W., Dowsett, H.J., Grebmeier, J.M., 2021. Biogeography and ecology of ostracoda in the US northern bering, Chukchi, and beaufort seas. PLoS One 16 (5), e0251164.
- Goñi, M.A., Yunker, M.B., O'Connor, A.E., Kuzyk, Z.Z., Gobeil, C., Macdonald, R.W., 2013. Distribution and sources of organic matter in surface marine sediments across the North American Arctic margin. J. Geophys. Res.: Oceans 118 (9), 4017-4035. https://doi.org/10.1002/jgrc.20286.
- Granger, J., Sigman, D.M., Gagnon, J., Tremblay, J.E., Mucci, A., 2018. On the properties of the arctic halocline and Deep water masses of the Canada basin from nitrate isotope ratios. J. Geophys. Res.: Oceans 123 (8). https://doi.org/10.1029/
- Hancock, G.J., Webster, I.T., Ford, P.W., Moore, W.S., 2000. Using Ra isotopes to examine transport processes controlling benthic fluxes into a shallow estuarine lagoon. Geochem. Cosmochim. Acta 64 (21), 3685-3699. https://doi.org/10.1016/ S0016-7037(00)00469-5
- Heiss, E.M., Fulweiler, R.W., 2016. Coastal water column ammonium and nitrite oxidation are decoupled in summer. Estuar. Coast Shelf Sci. 178, 110-119. https:// doi.org/10.1016/j.ecss.2016.06.002.
- Hersbach, H., Dee, D.J.E.N., 2016. ERA5 reanalysis is in production. ECMWF Newsl. 147 (7), 5-6.
- Itoh, M., Shimada, K., Kamoshida, T., McLaughlin, F., Carmack, E., Nishino, S., 2012. Interannual variability of pacific winter water inflow through Barrow canyon from 2000 to 2006. J. Oceanogr. 68 (4), 575-592. https://doi.org/10.1007/s10872-012-0120 - 1
- Jackson, J.M., Melling, H., Lukovich, J.V., Fissel, D., Barber, D.G., 2015. Formation of winter water on the Canadian Beaufort shelf; new insight from observations during 2009-2011. J. Geophys. Res. C Oceans 120 (6), 4090-4107. https://doi.org/ 10.1002/2015JC010812
- Jakobsson, M., 2002. Hypsometry and volume of the Arctic Ocean and its constituent seas. G-cubed 3 (5), 1-18. https://doi.org/10.1029/2001GC000302
- Jones, E.P., Anderson, L.G., 1986. On the origin of the chemical properties of the Arctic Ocean halocline. J. Geophys. Res. 91 (C9), 10759. https://doi.org/10.1029/ JC091iC09p10759
- Kadko, D., Muench, R., 2005. Evaluation of shelf-basin interaction in the western Arctic by use of short-lived radium isotopes: the importance of mesoscale processes. Deep-Sea Res. Part II Top. Stud. Oceanogr. 52 (24-26), 3227-3244. https://doi.org/ 10.1016/j.dsr2.2005.10.008.
- Kadko, D., Pickart, R.S., Mathis, J., 2008. Age characteristics of a shelf-break eddy in the western Arctic and implications for shelf-basin exchange. J. Geophys. Res. 113 (C2), C02018. https://doi.org/10.1029/2007JC004429.
- Kipp, L.E., Charette, M.A., Moore, W.S., Henderson, P.B., Rigor, I.G., 2018. Increased fluxes of shelf-derived materials to the central Arctic Ocean. Sci. Adv. 4 (1), 1-10. https://doi.org/10.1126/sciadv.aao1302.
- Kipp, L.E., Kadko, D.C., Pickart, R.S., Henderson, P.B., Moore, W.S., Charette, M.A., 2019. Shelf-basin interactions and water mass residence times in the Western Arctic Ocean: insights provided by radium isotopes. J. Geophys. Res.: Oceans 124 (5). https://doi.org/10.1029/2019JC014988, 2019JC014988.
- Kipp, L.E., Spall, M.A., Pickart, R.S., Kadko, D.C., Moore, W.S., Dabrowski, J.S., Charette, M.A., 2020. Observational and modeling evidence of seasonal trends in sediment-derived material inputs to the Chukchi Sea. J. Geophys. Res.: Oceans 125 (5), 1-13. https://doi.org/10.1029/2019jc016007.
- January 1) Ku, T.L., Luo, S., 2008. Chapter 9 Ocean Circulation/Mixing Studies with Decay-Series Isotopes. Radioactivity in the Environment. Elsevier. https://doi.org/ 10.1016/S1569-4860(07)00009-5
- Lecher, A.L., 2017. Groundwater discharge in the arctic: a review of studies and implications for biogeochemistry. Hydrology 4 (3), 41. https://doi.org/10.3390/ hydrology4030041.
- Lee, S.H., Stockwell, D., Whitledge, T.E., 2010. Uptake rates of dissolved inorganic carbon and nitrogen by under-ice phytoplankton in the Canada Basin in summer 2005. Polar Biol. 33 (8), 1027-1036. https://doi.org/10.1007/s00300-010-0781-4.
- Lewis, K.M., van Dijken, G.L., Arrigo, K.R., 2020. Changes in phytoplankton concentration now drive increased Arctic Ocean primary production. Science (New York, N.Y.) 369 (6500), 198-202. https://doi.org/10.1126/science.aay8380.

- Li, J., Pickart, R.S., Lin, P., Bahr, F., Arrigo, K.R., Juranek, L., Yang, X., 2020. The atlantic water boundary current in the Chukchi borderland and southern Canada basin. J. Geophys. Res.: Oceans. https://doi.org/10.1029/2020JC016197.
- Lilly, J.M., Rhines, P.B., Visbeck, M., Davis, R., Lazier, J.R., Schott, F., Farmer, D., 1999. Observing deep convection in the Labrador Sea during winter 1994/95. J. Phys. Oceanogr. 29 (8), 2065–2098.
- Lin, P., Pickart, R.S., Moore, G.W.K., Spall, M.A., Hu, J., 2019. Characteristics and dynamics of wind-driven upwelling in the Alaskan Beaufort Sea based on six years of mooring data. Deep-Sea Res. Part II Top. Stud. Oceanogr. 162, 79–92. https://doi. org/10.1016/j.dsr2.2018.01.002.
- Martin, T., Steele, M., Zhang, J., 2014. Seasonality and long-term trend of Arctic Ocean surface stress in a model. J. Geophys. Res.: Oceans 119 (3), 1723–1738. https://doi. org/10.1002/2013JC009425@10.1002/(ISSN)2169-9291. FAMOS1.
- Moore, W.S., 2000. Ages of continental shelf waters determined from 223Ra and 224Ra. J. Geophys. Res.: Oceans 105 (C9), 22117–22122. https://doi.org/10.1029/
- Moore, W.S., 2010. The effect of submarine groundwater discharge on the ocean. Ann. Rev. Mar. Sci 2, 59–88. https://doi.org/10.1146/annurev-marine-120308-081019.
- Moore, W.S., Arnold, R., 1996. Measurement of 223Ra and 224Ra in coastal waters using a delayed coincidence counter. J. Geophys. Res. C Oceans 101 (C1), 1321–1329. https://doi.org/10.1029/95JC03139.
- Moore, W.S., Reid, D.F., 1973. Extraction of radium from natural waters using manganese-impregnated acrylic fibers. J. Geophys. Res. 78 (36), 8880–8886. https://doi.org/10.1029/JC078i036p08880.
- Moore, W.S., Blanton, J.O., Joye, S.B., 2006. Estimates of flushing times, submarine groundwater discharge, and nutrient fluxes to Okatee Estuary, South Carolina. J. Geophys. Res.: Oceans 111 (9), 1–14. https://doi.org/10.1029/2005JC003041.
- Moore, W.S., Humphries, M.S., Benitez-Nelson, C.R., Pillay, L., Higgs, C., 2019. Transport of radium and nutrients through eastern South African beaches. J. Geophys. Res.: Oceans 124 (3), 2010–2027. https://doi.org/10.1029/2018JC014772.
- Mulligan, A.E., Charette, M.A., 2006. Intercomparison of submarine groundwater discharge estimates from a sandy unconfined aquifer. J. Hydrol. 327 (3–4), 411–425. https://doi.org/10.1016/J.JHYDROL.2005.11.056.
- Naidu, A.S., Mowatt, T.C., 1983. Sources and dispersal patterns of clay minerals in surface sediments from the continental-shelf areas off Alaska. Geol. Soc. Am. Bull. 94 (7), 841–854. https://doi.org/10.1130/0016-7606(1983)94<841:SADPOC>2.0.CO;
- Naidu, A.S., Cooper, L.W., Finney, B.P., Macdonald, R.W., Alexander, C., Semiletov, I.P., 2000. Organic carbon isotope ratio (813C) of Arctic Amerasian Continental shelf sediments. Int. J. Earth Sci. 89 (3), 522–532. https://doi.org/10.1007/ s005310000121
- Nikolopoulos, A., Pickart, R.S., Fratantoni, P.S., Shimada, K., Torres, D.J., Jones, E.P., 2009. The western Arctic boundary current at 152°W: structure, variability, and transport. Deep-Sea Res. Part II Top. Stud. Oceanogr. 56 (17), 1164–1181. https:// doi.org/10.1016/j.dsr2.2008.10.014.
- Pabi, S., van Dijken, G.L., Arrigo, K.R., 2008. Primary production in the Arctic Ocean, 1998-2006. J. Geophys. Res.: Oceans 113 (8). https://doi.org/10.1029/2007.IC004578
- Pacini, A., Moore, G.W.K., Pickart, R.S., Nobre, C., Bahr, F., Våge, K., Arrigo, K.R., 2019. Characteristics and transformation of pacific winter water on the Chukchi Sea shelf in late spring. J. Geophys. Res.: Oceans 124 (10), 7153–7177. https://doi.org/10.1029/2019JC015261.
- Padman, L., Erofeeva, S., 2004. A barotropic inverse tidal model for the Arctic Ocean. Geophys. Res. Lett. 31 (2).
- Pickart, R.S., 2004. Shelfbreak circulation in the alaskan Beaufort sea: mean structure and variability. J. Geophys. Res. C Oceans 109 (4), 1–14. https://doi.org/10.1029/ 2003JC001912.
- September 17) Pickart, R.S., Moore, G.W.K., Torres, D.J., Fratantoni, P.S., Goldsmith, R. A., Yang, J., 2009. Upwelling on the continental slope of the alaskan beaufort sea: storms, ice, and oceanographic response. J. Geophys. Res.: Oceans. https://doi.org/10.1029/2008JC005009. Blackwell Publishing Ltd.
- Pickart, R.S., Spall, M.A., Moore, G.W.K., Weingartner, T.J., Woodgate, R.A., Aagaard, K., Shimada, K., 2011. Upwelling in the alaskan Beaufort sea: atmospheric forcing and local versus non-local response. Prog. Oceanogr. 88 (1–4), 78–100. https://doi.org/10.1016/j.pocean.2010.11.005.
- Pickart, R.S., Spall, M.A., Mathis, J.T., 2013a. Dynamics of upwelling in the Alaskan Beaufort Sea and associated shelf-basin fluxes. Deep Sea Res. Oceanogr. Res. Pap. 76, 35–51. https://doi.org/10.1016/J.DSR.2013.01.007.
- Pickart, R.S., Schulze, L.M., Moore, G.W.K., Charette, M.A., Arrigo, K.R., van Dijken, G., Danielson, S.L., 2013b. Long-term trends of upwelling and impacts on primary productivity in the Alaskan Beaufort Sea. Deep-Sea Res. Part I Oceanogr. Res. Pap. 79, 106–121. https://doi.org/10.1016/j.dsr.2013.05.003.
- Pickart, R.S., Moore, G.W.K., Mao, C., Bahr, F., Nobre, C., Weingartner, T.J., 2016. Circulation of winter water on the Chukchi shelf in early Summer. Deep Sea Res. Part II Top. Stud. Oceanogr. 130, 56–75. https://doi.org/10.1016/J.DSR2.2016.05.001.
- Rainville, L., Lee, C.M., Woodgate, R.A., 2011. Impact of wind-driven mixing in the Arctic Ocean. Oceanography 24 (3), 136–145. https://doi.org/10.5670/ oceanog.2011.65.

- Reimnitz, E., Dethleff, D., Nürnberg, D., 1994. Contrasts in arctic shelf sea-ice regimes and some implications: beaufort sea versus laptev sea. Mar. Geol. 119 (3–4), 215–225. https://doi.org/10.1016/0025-3227(94)90182-1.
- Rodellas, V., Garcia-Orellana, J., Masqué, P., Font-Muñoz, J.S., 2015. The influence of sediment sources on radium-derived estimates of Submarine Groundwater Discharge. Mar. Chem. 171, 107–117. https://doi.org/10.1016/j. marchem. 2015.02.010.
- Rutgers van der Loeff, M.M., Key, R.M., Scholten, J., Bauch, D., Michel, A., 1995. 228Ra as a tracer for shelf water in the Arctic ocean. Deep-Sea Res. Part II 42 (6), 1533–1553. https://doi.org/10.1016/0967-0645(95)00053-4.
- Rutgers van der Loeff, M.M., Kühne, S., Wahsner, M., Höltzen, H., Frank, M., Ekwurzel, B., et al., 2003. 228Ra and 226Ra in the kara and laptev seas. Continent. Shelf Res. 23 (1), 113–124. https://doi.org/10.1016/S0278-4343(02)00169-3.
- Rutgers van der Loeff, M.M., Cai, P., Stimac, I., Bauch, D., Hanfland, C., Roeske, T., Moran, S.B., 2012. Shelf-basin exchange times of Arctic surface waters estimated from 228Th/228Ra disequilibrium. J. Geophys. Res.: Oceans 117 (3). https://doi. org/10.1029/2011JC007478.
- Rutgers van der Loeff, M.M., Kipp, L., Charette, M.A., Moore, W.S., Black, E., Stimac, I., et al., 2018. Radium isotopes across the Arctic Ocean show time scales of water mass ventilation and increasing shelf inputs. J. Geophys. Res.: Oceans 123 (7), 4853–4873. https://doi.org/10.1029/2018JC013888.
- Santos, I.R., Eyre, B.D., Huettel, M., 2012. The driving forces of porewater and groundwater flow in permeable coastal sediments: a review. Estuar. Coast Shelf Sci. 98, 1–15. https://doi.org/10.1016/j.ecss.2011.10.024.
- Schulze, L.M., Pickart, R.S., 2012. Seasonal variation of upwelling in the Alaskan Beaufort Sea: impact of sea ice cover. J. Geophys. Res.: Oceans 117 (6). https://doi. org/10.1029/2012JC007985.
- Shen, Y., Benner, R., Robbins, L.L., Wynn, J.G., 2016. Sources, distributions, and dynamics of dissolved organic matter in the Canada and makarov basins. Front. Mar. Sci. 3 https://doi.org/10.3389/fmars.2016.00198.
- Shi, X., Wei, L., Hong, Q., Liu, L., Wang, Y., Shi, X., Ye, Y., Cai, P., 2019. Large benthic fluxes of dissolved iron in China coastal seas revealed by 224Ra/228Th disequilibria. Geochem. Cosmochim. Acta 260, 49–61. https://doi.org/10.1016/j. gca.2019.06.026.
- Shiozaki, T., Ijichi, M., Fujiwara, A., Makabe, A., Nishino, S., Yoshikawa, C., Harada, N., 2019. Factors regulating nitrification in the Arctic Ocean: potential impact of sea ice reduction and ocean acidification. Global Biogeochem. Cycles 33 (8), 1085–1099. https://doi.org/10.1029/2018GB006068.
- Smith, J.N., Moran, S.B., Macdonald, R.W., 2003. Shelf-basin interactions in the Arctic Ocean based on 210Pb and Ra isotope tracer distributions. Deep-Sea Res. Part I Oceanogr. Res. Pap. 50 (3), 397–416. https://doi.org/10.1016/S0967-0637(02) 00166-8.
- Tremblay, J.É., Michel, C., Hobson, K.A., Gosselin, M., Price, N.M., 2006. Bloom dynamics in early opening waters of the Arctic Ocean. Limnol. Oceanogr. 51 (2), 900–912. https://doi.org/10.4319/lo.2006.51.2.0900.
- Trimble, S.M., Baskaran, M., Porcelli, D., 2004. Scavenging of thorium isotopes in the Canada basin of the Arctic Ocean. Earth Planet Sci. Lett. 222 (3–4), 915–932. https://doi.org/10.1016/j.epsl.2004.03.027.
- https://doi.org/10.1016/j.epsl.2004.03.027.
 Vieira, L.H., Achterberg, E.P., Scholten, J., Beck, A.J., Liebetrau, V., Mills, M.M., Arrigo, K.R., 2019. Benthic fluxes of trace metals in the Chukchi Sea and their transport into the Arctic Ocean. Mar. Chem. 208, 43–55. https://doi.org/10.1016/j.marchem.2018.11.001.
- Walsh, J.E., 1978. Temporal and spatial scales of the arctic circulation. Mon. Weather Rev. 106. American Meteorological Society. https://doi.org/10.1175/1520-0493 (1978)106<1532:TASSOT>2.0.CO;2.
- Walvoord, M.A., Kurylyk, B.L., 2016. Hydrologic impacts of thawing permafrost—a review. Vadose Zone J. 15 (6), 1–20. https://doi.org/10.2136/vzj2016.01.0010. Webster, I.T., Hancock, G.J., Murray, A.S., 1995. Modelling the effect of salinity on
- Webster, I.T., Hancock, G.J., Murray, A.S., 1995. Modelling the effect of salinity on radium desorption from sediments. Geochem. Cosmochim. Acta 59 (12), 2469–2476. https://doi.org/10.1016/0016-7037(95)00141-7.
- Wei, L., Cai, P., Shi, X., Cai, W.J., Liu, W., Hong, Q., Wu, T., Bai, Y., Cheng, P., Sun, Z., 2021. Winter mixing accelerates decomposition of sedimentary organic carbon in seasonally hypoxic coastal seas. Geochem. Cosmochim. Acta. https://doi.org/ 10.1016/j.gca.2021.11.003.
- Weingartner, T.J., Cavalieri, D.J., Aagaard, K., Sasaki, Y., 1998. Circulation, dense water formation, and outflow on the northeast Chukchi shelf. J. Geophys. Res. C Oceans 103 (3334), 7647–7661. https://doi.org/10.1029/98jc00374.
- Weingartner, T.J., Danielson, S.L., Potter, R.A., Trefry, J.H., Mahoney, A., Savoie, M., et al., 2017. Circulation and water properties in the landfast ice zone of the Alaskan Beaufort Sea. Continent. Shelf Res. 148, 185–198. https://doi.org/10.1016/j.csr.2017.09.001.
- Williams, W.J., Carmack, E.C., 2015. The "interior" shelves of the Arctic Ocean: physical oceanographic setting, climatology and effects of sea-ice retreat on cross-shelf exchange. Prog. Oceanogr. 139, 24–41. https://doi.org/10.1016/j.pocean.2015.07.008.